

Contents lists available at ScienceDirect

Journal of Computational Physics

www.elsevier.com/locate/jcp



Sequential local mesh refinement solver with separate temporal and spatial adaptivity for non-linear two-phase flow problems



Hanyu Li*, Wing Tat Leung, Mary F. Wheeler

Center for Subsurface Modeling, The University of Texas at Austin, Austin, TX 78712, United States of America

ARTICLE INFO

Article history:

Received 1 April 2019 Received in revised form 6 September 2019 Accepted 28 October 2019 Available online 31 October 2019

Keywords:

Space-time domain decomposition Mixed finite element method Sequential local mesh refinement Iterative solver Non-linear system

ABSTRACT

Convergence failure and slow convergence rates are among the biggest challenges with solving the system of non-linear equations numerically. Although mitigated, such issues still linger when using strictly small time steps and unconditionally stable fully implicit schemes. The price that comes with restricting time steps to small scales is the enormous computational load, especially in large-scale models. To address this problem, we introduce a sequential local mesh refinement framework of temporal and spatial adaptivity to optimize convergence rate and prevent convergence failure, while not restricting the whole system to small time steps, thus improving computational efficiency. Two types of error estimators are introduced to estimate the spatial discretization error, the temporal discretization error separately. These estimators provide a global upper bounds on the dual norm of the residual and the non-conformity of the numerical solution for non-linear two phase flow models. The mesh refinement algorithm starts from solving the problem on the coarsest space-time mesh, then the mesh is refined sequentially based on the spatial error estimator and the temporal error estimator. After each refinement, the solution from the previous mesh is used to estimate the initial guess of unknowns on the current mesh for faster convergence. Numerical results are presented to confirm accuracy of our algorithm as compared to the uniformly fine time step and fine spatial discretization solution. We observe around 25 times speedup in the solution time by using our algorithm.

© 2019 Elsevier Inc. All rights reserved.

1. Introduction

Complex multiphase flow and reactive transport in subsurface porous media is mathematically modeled by systems of non-linear equations. Due to significant non-linearity, solving such systems with Newton's method frequently suffers from convergence issues even when applying very small time steps and using unconditionally stable fully implicit schemes. This problem becomes much more severe in large-scale models since significant increases in the number of unknowns makes each Newton iteration computationally intensive. However, by reducing the size of the model using multiscale techniques and optimizing convergence rates of Newton's method, one can achieve orders of magnitude improvement in computational efficiency.

E-mail addresses: lihanyu234@ices.utexas.edu (H. Li), wleung@ices.utexas.edu (W.T. Leung), mfw@ices.utexas.edu (M.F. Wheeler).

^{*} Corresponding author.

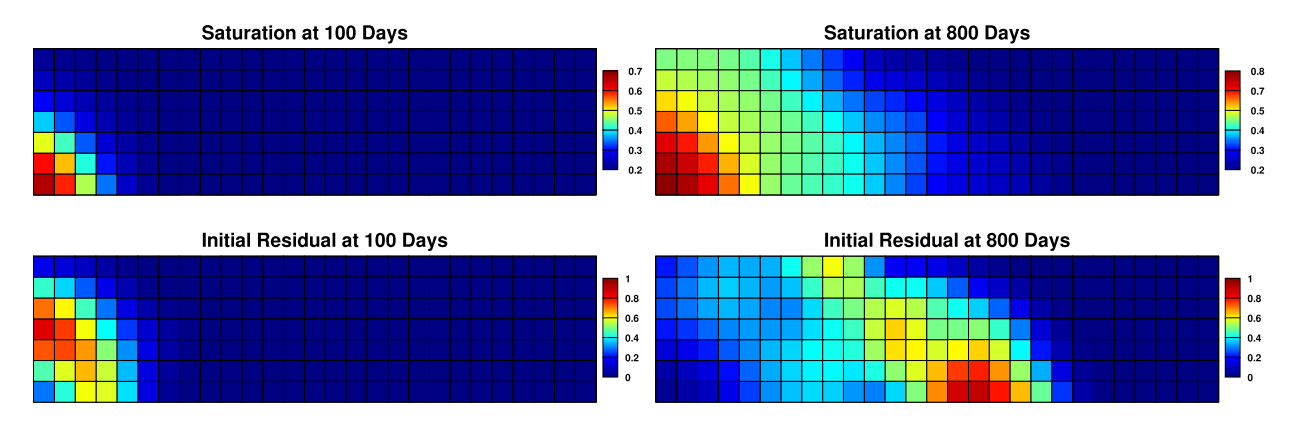


Fig. 1. Saturation and normalized initial non-linear residual at 100 and 800 days. (For interpretation of the colors in the figures, the reader is referred to the web version of this article.)

Adaptive homogenization [4,32] reduces the number of unknowns in the model by replacing fine mesh with coarse mesh in regions where non-linearity and variable (for example saturation) variation is negligible. However, fine and coarse discretization in space requires different time scales for stable numerical solutions. Forcing the coarse mesh to accommodate the fine mesh by taking fine time steps fails to reduce the number of unknowns in time. Space-time domain decomposition addresses this difficulty by allowing different time scales for different spatial grids.

Many space-time domain decomposition approaches have been proposed in the past. In [1,22,23], space-time finite elements were introduced for elastodynamics with discontinuous Galerkin (DG) in time. The space time method has also been applied to reaction-diffusion problems with different time discretization schemes [7,8,25–27,29]. Other examples include [19] who have applied space time sparse grids for parabolic problems; [40] who applied local time stepping based on multiplicative Schwarz domain decomposition; [36] who formulated local time stepping for fluid dynamics and fluid structure interactions.

The aforementioned literature applied space-time domain decomposition methods to Galerkin based schemes and did not consider multiphase flow in subsurface porous media. Prior work on mixed finite element (MFE) methods focused on linear single phase flow and transport problems where flow is naturally decoupled from advection-diffusion transport [20,21]. In the latter, an optimized Schwarz waveform relaxation (OSWR) based on Robin transmission was employed. In [35], a space-time approach for non-linear coupled multiphase flow and transport problems was formulated on a static grid using an enhanced velocity method, a MFE variant [2,3,5,37,39]. Here continuity of fluxes at non-matching space-time interfaces was strongly enforced unlike the iterative solution scheme introduced in [20], that require subdomain problems to be solved iteratively until weak continuity of fluxes is satisfied at interfaces. In addition adaptive mesh refinement was introduced in [34], thus improving computational efficiency while maintaining accuracy. Further enhancements included applying an initial residual as an inexpensive error estimator to search for regions requiring refinement. As an example of this approach we observe from Fig. 1, that the normalized non-linear residual becomes the largest in regions with the highest non-linearity (water saturation front), thus resulting in increased computational time. Refining such regions in time ensures Newtonian convergence while refining in space maintains solution accuracy.

The adaptive local mesh refinement approach demonstrated in [34] allowed only one level of refinement in both space and time, thus restricting the largest coarse time step allowed for stable numerical convergence. This approach was extended in [30] by allowing additional refinement levels, similar to the algorithm introduced in [10], in which only spatial adaptivity was treated. When solving problems on each coarse space-time domain, regions with large non-linear residual and saturation variation are sequentially refined to the finest resolution to ensure solution convergence and accuracy. After each refinement, before solving the problem on the new mesh, the initial guess for the unknowns are populated by the solution on the previous mesh using linear projections. The initial guess then obtained becomes a better approximation to the true solution. Therefore, the non-linear solver convergence is not only guaranteed, but also accelerated. Although achieving 5 times speedup of solution time with an iterative linear solver, results in [30] relied on isotropic space-time refinements which produced a significant number of unnecessary elements. Regions with large saturation variation behind the front are forced to take redundant fine time steps. Preventing such over-refinement further improves computational performance. Another problem associated with isotropic refinement schemes is that, the error indicator used to pinpoint refinement location combines both temporal and spatial saturation variations. Error indicators calculated in this fashion often mislead the refinement process, especially in channelized permeability fields. In this work, we have extended the method demonstrated in [30] by separating temporal and spatial adaptivity to further improve computational performance and solution accuracy. Further improvement involves the development of error estimators and bounds for a well-known metric first proposed in [38] for two phase flow problems.

The novelty of this work is the application of a space-time algorithm to nonlinear multiphase flow that is based on error estimates that provide global upper bounds for the dual norm of the residual and the non-conformity of the numerical solution. This approach does require the reconstruction of fluxes.

In this paper, we restrict ourselves to non-linear two-phase flow problems in subsurface porous media. The rest of the paper begins by describing the governing equations for two phase flow, the functional spaces for space-time domain decomposition, the enhanced velocity weak variational formulation in Section 2. Analysis of error estimator used in the refinement process is presented in Section 3 followed by description of the algorithm for the sequential local mesh refinement solver in Section 4. Results from three numerical experiments using the proposed algorithm are discussed in Section 5. One of the examples presented involves compressible two-phase flow, which is a critical step in studying three phase problems.

2. Two phase flow formulation

We consider the following well-known two-phase, slightly compressible flow in porous medium model, with oil and water phase mass conservation, constitutive equations, boundary and initial conditions.

$$\frac{\partial (\phi \rho_{\alpha} s_{\alpha})}{\partial t} + \nabla \cdot \boldsymbol{u}_{\alpha} = q_{\alpha} \quad \text{in } \Omega \times J$$
(2.1)

$$\mathbf{u}_{\alpha} = -K \rho_{\alpha} \frac{k_{r\alpha}}{\mu_{\alpha}} (\nabla p_{\alpha} - \rho_{\alpha} \mathbf{g}) \quad \text{in } \Omega \times J$$
(2.2)

$$\mathbf{u}_{\alpha} \cdot \mathbf{v} = 0 \quad \text{on } \partial\Omega \times J \tag{2.3}$$

$$\begin{cases} p_{\alpha} = p_{\alpha}^{0} \\ s_{\alpha} = s_{\alpha}^{0} \end{cases} \text{ at } \Omega \times \{t = 0\}$$
 (2.4)

 ϕ is porosity and K is permeability tensor. ρ_{α} , s_{α} , u_{α} and q_{α} are density, saturation, velocity and source/sink, respectively for each phase. The phases are slightly compressible and the phase densities are calculated by Eqn. (2.5),

$$\rho_{\alpha} = \rho_{\alpha,ref} \cdot e^{c_{f,\alpha}(p_{\alpha} - p_{\alpha,ref})} \tag{2.5}$$

with $c_{f,\alpha}$ being the fluid compressibility and $\rho_{\alpha,ref}$ being the reference density at reference pressure $p_{\alpha,ref}$. In the constitutive equation (2.2) given by Darcy's law, $k_{r\alpha}$, μ_{α} and p_{α} are the relative permeability, viscosity and pressure for each phase. Relative permeability is a function of saturation. Pressure differs between wetting phase and non-wetting phase in the presence of capillary pressure, which is also a function of saturation.

$$k_{r\alpha} = f(s_{\alpha}) \tag{2.6}$$

$$p_c = g(s_\alpha) = p_{nw} - p_w \tag{2.7}$$

The saturation of all phases obeys the constrain (2.8).

$$\sum_{\alpha} s_{\alpha} = 1 \tag{2.8}$$

The boundary and initial conditions are given by Eqn. (2.3) and (2.4). J = (0, T] is the time domain of interest while Ω is the spatial domain.

Now we will give a brief introduction of enhanced velocity formulation in space-time domain. Let J=(0,T] be partitioned in to a number of coarse time intervals $\{t_n\}_{n=1}^N$ where $0=t_1< t_2<\cdots< t_N=T$. $J_n=(t_n,t_{n+1}]$ is the nth partition of the time domain of interest. Consider $J_n\times\Omega$ as an union of some non-overlapping subdomains $\{I_i\times\Omega_i\}$, namely $J_n\times\Omega=\cup_i (I_i\times\Omega_i)$, where $I_i=(\tau_i,\tau_{i+1}]$ is a sub-interval of $J_n=(t_n,t_{n+1}]$ and Ω_i is a subdomain of Ω . The interfaces of the subdomains are defined as $\Gamma_{i,j}=\partial \left(I_i\times\Omega_i\right)\cap\partial \left(I_j\times\Omega_j\right)$, $\Gamma=\cup_{i,j}\Gamma_{i,j}$ and $\Gamma_i=\Gamma\cap\partial \left(I_i\times\Omega_i\right)$. We use space-time enhanced velocity method similar as [39] to discretize the system. The functional spaces for mixed weak formulation are

$$\boldsymbol{V} = H(div;\Omega) = \left\{\boldsymbol{v} \in \left(L^2(\Omega)\right)^d : \nabla \cdot \boldsymbol{v} \in L^2(\Omega)\right\}, \quad W = L^2(\Omega),$$

with finite dimensional subspaces as V_h and W_h . Let $\mathcal{T}_{h,i}^n$ be a rectangular partition of $I_i \times \Omega_i$, $E_i^m = T_i^m \times F_i^m$ be an space-time element in such partition with $T_i^m = (\tau_{i,0}^m, \tau_{i,1}^m]$ and $\mathcal{T}_h^n = \cup_i \mathcal{T}_{h,i}^n$. Define velocity and pressure/saturation spaces as

$$\begin{aligned} & \boldsymbol{V}_{h,i}^{n} = \left\{ \boldsymbol{v} \in L^{2} \Big(I_{i}; H(div; \Omega_{i}) \Big) : \boldsymbol{v}(\cdot, \boldsymbol{x}) \Big|_{F_{i}^{m}} \in \boldsymbol{V}_{h}(F_{i}^{m}) \text{ and } \boldsymbol{v}(t, \cdot) \Big|_{T_{i}^{m}} = \sum_{a=1}^{l} \boldsymbol{v}_{a} t^{a} \text{ with } \boldsymbol{v}_{a} \in \boldsymbol{V}_{h}(F_{i}^{m}), \forall E_{i}^{m} \in \mathcal{T}_{h,i}^{n} \right\}, \\ & W_{h,i}^{n} = \left\{ w \in L^{2} \Big(I_{i}; L^{2}(\Omega_{i}) \Big) : w(\cdot, \boldsymbol{x}) \Big|_{F_{i}^{m}} \in W_{h}(F_{i}^{m}) \text{ and } w(t, \cdot) \Big|_{T_{i}^{m}} = \sum_{a=1}^{l} w_{a} t^{a} \text{ with } w_{a} \in W_{h}(F_{i}^{m}), \forall E_{i}^{m} \in \mathcal{T}_{h,i}^{n} \right\}, \end{aligned}$$

where

$$\mathbf{V}_h(F_i^m) = \left\{ \mathbf{v} = (v_1, v_2) \text{ or } \mathbf{v} = (v_1, v_2, v_3) : v_l = \alpha_l + \beta_l x_l; \ \alpha_l, \beta_l \in \mathbb{R}, l = 1, \cdots, d \right\}$$

$$W_h(F_i^m) = \left\{ w \text{ is a constant in } F_i^m \right\}$$

Functions in $\boldsymbol{V}_{h,i}^n$ and $W_{h,i}^n$ along time dimension are represented by polynomials with degrees up to l. As described in [35], following the discontinuous Galerkin (DG) discretization in time [6,24], the DG_0 (polynomial of degree zero) scheme makes $\boldsymbol{v}(t,\cdot)|_{T_i^m}$ and $w(t,\cdot)|_{T_i^m}$ constant. Then we define the product spaces as $\boldsymbol{V}_h^n = \bigoplus_i \boldsymbol{V}_{h,i}^n$. We remark that \boldsymbol{V}_h^n is not a subspace of \boldsymbol{V} . To obtain a finite element space containing basis functions with continuous normal flux, we need to modify the basis functions on the space-time interface $\Gamma_{i,j}$. Let $\mathcal{E}_{h,i,j}^n$ be the rectangular partition of $\Gamma_{i,j}$ obtained from the intersection of the traces of $\mathcal{T}_{h,i}^n$ and $\mathcal{T}_{h,j}^n$. For each $e \in \mathcal{E}_{h,i,j}^n$, we define a RT_0 basis function \boldsymbol{v}_e with a normal component equal to one on e, namely $\boldsymbol{v}_e|_e \cdot \boldsymbol{v} = 1$. We then define the space \boldsymbol{V}_h^Γ to be the span of all these basis function, \boldsymbol{v}_e . Then the space-time mixed finite element velocity space $\boldsymbol{V}_h^{n,*}$ is

$$\boldsymbol{V}_{h}^{n,*} = \left(\bigoplus_{i} \boldsymbol{V}_{h,i}^{n,0} \right) \bigoplus \boldsymbol{V}_{h}^{\Gamma}$$

where $V_{h,i}^{n,0}$ is the subspace of $V_{h,i}^n$ with zero normal component on Γ_i . Similarly, the pressure/saturation space is $W_h^n = \bigoplus_i W_{h,i}^n$.

Now consider any function f piecewise in time (for example functions in $\mathbf{V}_h^{n,*}$ and W_h^n), define f_{τ} as the linear interpolation along time direction as

$$\left. f_{\tau}(t,\cdot) \right|_{(\tau_{i,0}^m,\tau_{i,1}^m] \times F_i^m} = \frac{t - \tau_{i,0}^m}{\tau_{i,1}^m - \tau_{i,0}^m} f(\tau_{i,1}^{m,-},\cdot) \right|_{F_i^m} + \frac{\tau_{i,1}^m - t}{\tau_{i,1}^m - \tau_{i,0}^m} f(\tau_{i,0}^{m,-},\cdot) \Big|_{F_i^m}, \ \forall E_i^m = T_i^m \times F_i^m \in \mathcal{T}_h^m$$

and we have

$$\int\limits_{\tau_{i,0}^{m}}^{\tau_{i,1}^{m}} \partial_{t} f_{\tau}(t,\cdot) \Big|_{F_{i}^{m}} = f(\tau_{i,1}^{m},\cdot) \Big|_{F_{i}^{m}} - f(\tau_{i,0}^{m},\cdot) \Big|_{F_{i}^{m}}$$

To simplify the notation, let $C_{\alpha,h}^n = \rho_{\alpha} \left(p_{\alpha,h}^n \right) s_{\alpha,h}^n$ be the phase mass concentration. Then space-time enhanced velocity method formulates Eqn. (2.1) and (2.2) as: find $\boldsymbol{u}_{\alpha,h}^n \in \boldsymbol{V}_h^{n,*}$, $\tilde{\boldsymbol{u}}_{\alpha,h}^n \in \boldsymbol{V}_h^{n,*}$, $s_{\alpha,h}^n \in W_h^n$, $p_{\alpha,h}^n \in W_h^n$ such that

$$\int_{I_{n}} \int_{\Omega} \partial_{t} \left(\phi C_{\alpha,h,\tau}^{n} \right) w + \int_{I_{n}} \int_{\Omega} \left(\nabla \cdot \boldsymbol{u}_{up,\alpha,h}^{n} \right) w = \int_{I_{n}} \int_{\Omega} q_{\alpha} w \quad \forall w \in W_{h}^{n}$$
(2.9)

$$\int_{I_n} \int_{\Omega} K^{-1} \tilde{\boldsymbol{u}}_{\alpha,h}^n \cdot \boldsymbol{v} = \int_{I_n} \int_{\Omega} p_{\alpha,h}^n \nabla \cdot \boldsymbol{v} \quad \forall \boldsymbol{v} \in \boldsymbol{V}_h^{n,*}$$
(2.10)

$$\int_{I_n} \int_{\Omega} \boldsymbol{u}_{\alpha,h}^n \cdot \boldsymbol{v} = \int_{I_n} \int_{\Omega} \lambda_{\alpha} \tilde{\boldsymbol{u}}_{\alpha,h}^n \cdot \boldsymbol{v} \quad \forall \boldsymbol{v} \in \boldsymbol{V}_h^{n,*}$$
(2.11)

The mobility ratio in (2.11) is defined as

$$\lambda_{\alpha} = \frac{k_{r\alpha}\rho_{\alpha}}{\mu_{\alpha}} \tag{2.12}$$

and $oldsymbol{u}_{un,\alpha,h}^n$ is the upwind velocity calculated by

$$\int_{I_{n}} \int_{\Omega} \boldsymbol{u}_{up,\alpha,h}^{n} \cdot \boldsymbol{v} = \int_{I_{n}} \int_{\Omega} \lambda_{\alpha}^{*} \tilde{\boldsymbol{u}}_{\alpha,h}^{n} \cdot \boldsymbol{v} \quad \forall \boldsymbol{v} \in \boldsymbol{V}_{h}^{n,*}$$
(2.13)

The additional auxiliary phase fluxes $\tilde{\boldsymbol{u}}_{\alpha,h}^n$ is used to avoid inverting zero phase relative permeability [31]. Calculation of the upwind mobility ratio λ_{α}^* is referred to Eqn. (A.19). The variational form for specifically oil-water system and its fully discrete formulation is attached in Appendix A. The discrete formulation provides us a non-linear system of equations for pressure and saturation. We approximate such system in linear form and use Newton iteration to approach the true solution. Depending on the level of non-linearity and the closeness between the initial guess and the true solution, Newton's method could take numerous iterations before achieving convergence. We will use the sequential local mesh refinement algorithm to accelerate the Newtonian convergence. Before introducing refinement algorithm, in the next section, we will first present analysis for error estimator used for searching refinement regions.

3. A posteriori error estimate

In this section, we discuss the error estimate analysis as an extension to the work presented in [38]. In contrast to the previous work, our approach to calculate a posteriori error estimate does not rely on computationally expensive local reconstruction of fine scale solution from coarse scale solution. Let $E^m_i = (\tau^m_{i,0}, \tau^m_{i,1}] \times F^m_i \in \mathcal{T}^n_h$ be a space-time element, we define local error estimators $\eta^{n,m}_{t,r,\alpha,i}, \eta^{n,m}_{s,r,\alpha,i}, \eta^{n,m}_{t,f,\alpha,i}, \eta^{n,m}_{s,f,\alpha,i}, \eta^{n,m}_{t,p,\alpha,i}, \eta^{n,m}_{s,p,\alpha,i}$ as follows

$$\eta_{t,r,\alpha,i}^{n,m} = \left| \tau_{i,1}^m - \tau_{i,0}^m \right| \left(\int\limits_{F_m^m} \left| \partial_t \left(\phi C_{\alpha,h,\tau}^n \right) + \nabla \cdot \boldsymbol{u}_{up,\alpha,h,\tau}^n - q_\alpha \right|^2 \right)^{\frac{1}{2}}$$

$$(3.1)$$

$$\eta_{s,r,\alpha,i}^{n,m} = \left| F_i^m \right| \left(\int\limits_{E_i^m} \left| \partial_t \left(\phi C_{\alpha,h,\tau}^n \right) + \nabla \cdot \boldsymbol{u}_{up,\alpha,h,\tau}^n - q_\alpha \right|^2 \right)^{\frac{1}{2}}$$

$$(3.2)$$

$$\eta_{t,f,\alpha,i}^{n,m} = \left(\int_{E_{m}^{m}} K^{-1} \left| \boldsymbol{u}_{\alpha,h}^{n} - \boldsymbol{u}_{\alpha,h,\tau}^{n} \right|^{2} \right)^{\frac{1}{2}}$$
(3.3)

$$\eta_{s,f,\alpha,i}^{n,m} = \left(\int_{F^m} K^{-1} \left| \mathbf{u}_{up,\alpha,h}^n - \mathbf{u}_{\alpha,h}^n \right|^2 \right)^{\frac{1}{2}}$$
(3.4)

$$\eta_{t,p,\alpha,i}^{n,m} = \left(\int\limits_{E_i^m} K^{-1} \left| \partial_t \tilde{\boldsymbol{u}}_{\alpha,h,\tau}^n \right|^2 \right)^{\frac{1}{2}} \tag{3.5}$$

$$\eta_{s,p,\alpha,i}^{n,m} = \left(\left| E_i^m \right|^2 \int\limits_{E_i^m} \left| \nabla \times \left(K^{-1} \tilde{\boldsymbol{u}}_{\alpha,h}^n \right) \right|^2 + \sum_{e \in \partial E_i^m} |e| \int\limits_{e} \left[\left(K^{-1} \tilde{\boldsymbol{u}}_{\alpha,h}^n \right) \times \boldsymbol{n}_e \right]^2 \right)^{\frac{1}{2}}$$

$$(3.6)$$

Eqn. (3.1)-(3.2) are residual estimators, Eqn. (3.3)-(3.4) are flux estimators and Eqn. (3.5)-(3.6) are non-conformity estimators. Eqn. (3.1) through (3.6) will provide upper bound for the error measure we are about to introduce. It is common to use energy norm as an error measurement for linear problems. However, it is much more complicated for nonlinear problems. Instead we use the dual norm of the residual, which is also widely applied, as our error measure. We denote

$$X^n = L^2\left(J_n; H^1(\Omega)\right) \bigcap H^1\left(J_n; L^2(\Omega)\right)$$

and for any $\psi \in X^n$

$$\|\psi\|_{X^{n}} = \int_{L_{n}} \left(\|\psi\|_{L^{2}(\Omega)}^{2} + \|K^{\frac{1}{2}}\nabla\psi\|_{L^{2}(\Omega)}^{2} + \|\psi_{t}\|_{L^{2}(\Omega)}^{2} \right).$$

Let s_{α}^{n} , p_{α}^{n} , u_{α}^{n} and $s_{\alpha,h}^{n}$, $p_{\alpha,h}^{n}$, $u_{\alpha,h}^{n}$ be the exact and numerical saturation, pressure and velocities solutions. The error measure $\|\cdot\|$ is defined as

$$|||(s_{\alpha}^{n}-s_{\alpha,h}^{n},p_{\alpha}^{n}-p_{\alpha,h}^{n},\tilde{\boldsymbol{u}}_{\alpha}^{n}-\tilde{\boldsymbol{u}}_{\alpha,h}^{n})|||:=N_{\alpha}^{n}+N_{\alpha,p}^{n}$$

where

$$N_{\alpha}^{n} = \sup_{\psi \in X^{n}, \|\psi\| = 1} \left\{ \int_{I_{n}} \left(\int_{\Omega} \partial_{t} \left(\phi C_{\alpha,h}^{n} - \phi C_{\alpha,h,\tau}^{n} \right) \psi - \int_{\Omega} \left(\mathbf{u}_{\alpha,h}^{n} - \mathbf{u}_{\alpha,h,\tau}^{n} \right) \cdot \nabla \psi \right) \right\},$$

and

$$N_{\alpha,p}^{n} = \inf_{\psi \in X^{n}} \left\{ \int_{L_{\infty}} \int_{\Omega} K^{-1} \left(\tilde{\boldsymbol{u}}_{\alpha,h,\tau}^{n} + K \nabla \psi \right)^{2} \right\}^{\frac{1}{2}}$$

 N_{α}^{n} represents the dual norm of the residual and $N_{\alpha,p}^{n}$ measures the non-conformity of the numerical solutions.

Lemma 1. There exist a subspace $M_h^{n,*} \subset L^2(J_n; H(curl, \Omega))$ such that

$$\nabla \times M_h^{n,*} \subset \mathbf{V}_h^{n,*} \cap L^2(J_n; H(div, \Omega)).$$

Moreover, for all $v \in L^2(J_n; H(curl, \Omega))$, there exist $\Pi_{M_h^{n,*}}(v) \in M_h^{n,*}$ such that

$$\begin{split} & \sum_{E_i^m \in \mathcal{T}_h^n} \left\| v - \Pi_{M_h^{n,*}}(v) \right\|_{L^2(E_i^m)} \leq C \sum_{E_i^m \in \mathcal{T}_h^n} \left| E_i^m \right| \left\| \nabla v \right\|_{L^2(E_i^m)} \\ & \sum_{e \in \mathcal{E}_h^n} |e|^{-1} \left\| v - \Pi_{M_h^{n,*}}(v) \right\|_{L^2(e)}^2 \leq C \sum_{e \in \mathcal{E}_h^n} \left\| v \right\|_{H^{1/2}(e)}^2 \end{split}$$

where \mathcal{E}_h^n is the set of space-time edge.

Proof. We will first construct the space $M_h^{n,*}$ for d=2. For a sub-domain $I_i \times \Omega_i$, we will define a space $M_{h,i}^n \subset L^2(I_i; H(curl, \Omega_i))$ by

$$M_{h,i}^{n} = \left\{ v \in L^{2} \left(I_{i}; H(curl, \Omega_{i}) \right) : v \big|_{E_{i}^{m}}(t, x) = (\alpha_{1}x_{1} + \beta_{1})(\alpha_{2}x_{2} + \beta_{2}) \right\}$$

We next define the product space as $M_h^n = \bigoplus_i M_{h,i}^n$. We remark that M_h^n is not a subspace of $L^2 \Big(J_n; H(curl, \Omega) \Big)$. To obtain a space-time finite element space $M_h^{n,*}$ in $L^2 \Big(J_n; H(curl, \Omega) \Big)$, we require $v \times v_e$ to be continuous for all $v \in M_h^{n,*}$, for each edge e on the space-time interface. For each space-time interface $\Gamma_{i,j}$, we have the normal vector $v_{\Gamma_{i,j}}$ of $\Gamma_{i,j}$ satisfies $v_{\Gamma_{i,j}} = \hat{e}_l$ for some $l \leq d$ where $\{\hat{e}_l\}$ is the standard basis of \mathbb{R}^d . Let $\mathcal{V}_{i,j}$ be the set of all vertices on $\Gamma_{i,j}$. For each $x \in \mathcal{V}_{i,j}$, we can define a bi-linear function v_x with $v_x(x) = 1$ and $v_x(y) = 0$ for $y \in \mathcal{V}_{i,j}$. We then define the space M_h^{Γ} to be the span of all these basis functions v_x . Then we define $M_h^{n,*}$ as

$$M_h^{n,*} = \left(\bigoplus_i M_{h,i}^{n,0} \right) \bigoplus M_h^{\Gamma}$$

where $M_{h,i}^{n,0}$ is the subspace of $M_{h,i}^n$ with zero trace on boundary of Ω_i .

For each $v \in M_h^{n,*}$, since v is piecewise bi-linear, we obtain $\nabla \times v\big|_{E_i^m} = (\partial_2 v - \partial_1 v)\big|_{E_i^m} \in RT_0$ for all $E_i^m \in \mathcal{T}_h^n$ and v can be written a sum of bi-linear basis functions v_x , since v_x can be written in a tensor form, we have $\partial_i v \cdot \hat{e}_j$ for $j \neq i$. We then obtain $\nabla \times v_x \in V_h^{n,*}$ and thus, we have $\nabla \times v \in V_h^{n,*}$. We consider the Clément interpolation operator $\Pi_{M_h^{n,*}}$ defined as

$$\Pi_{M_h^{n,*}}(u) = \sum_{x \in \mathcal{V}_h} \left(|\omega_x|^{-1} \int_{\omega_x} u \right) v_x$$

where \mathcal{V}_h is a set of all vertices of \mathcal{T}_h^n , v_x is the nodal basis functions corresponding to vertex x and ω_x is the union of space-time element sharing vertex x. Since $\{v_x\}_{x\in\mathcal{V}_h}$ is a partial of unity of $J_n\times\Omega$, we have $\Pi_{M_h^{n,*}}(v)\in M_h^{n,*}$ such that

$$\begin{aligned} & \left\| v - \Pi_{M_{h}^{n,*}}(v) \right\|_{L^{2}(E_{i}^{m})} \leq C \left| E_{i}^{m} \right| \left\| \nabla v \right\|_{L^{2}(E_{i}^{m})} \quad \forall E_{i}^{m} \in \mathcal{T}_{h}^{m} \\ & \left\| v - \Pi_{M_{h}^{n,*}}(v) \right\|_{L^{2}(e)}^{2} \leq C \left| e \right| \left\| v \right\|_{H^{1/2}(e)}^{2} \quad \forall e \in \partial E_{i}^{m} \end{aligned}$$

For d = 3, we can consider $M_{h,i}^n$ defined as

$$M_{h,i}^{n} = \left\{ v = (v_1, v_2, v_3) \in L^2(I_i; H(curl, \Omega_i)) : v_l|_E(t, x) = \prod_{j \neq l} (\alpha_j x_j + \beta_j) \right\}$$

Using a similar trick, we can modify the space on the interface and obtain the lemma. \Box

Next, we will present a posteriori error estimate for this error measure. In the following lemma, we estimate the dual norm of the residual of the mass balance equations.

Lemma 2. Let $\eta_{t,r,\alpha,i}^{n,m}$, $\eta_{s,r,\alpha,i}^{n,m}$, $\eta_{t,f,\alpha,i}^{n,m}$ and $\eta_{s,f,\alpha,i}^{n,m}$ be the error indicators defined in Eqn. (3.1)-(3.4). There exist constants C, $C_{poin} > 0$ such that

$$N_{\alpha}^{n} \leq \left(\sum_{E_{i}^{m} \in \mathcal{T}_{h}^{n}} \left(\eta_{t,f,\alpha,i}^{n,m}\right)^{2}\right)^{\frac{1}{2}} + \left(\sum_{E_{i}^{m} \in \mathcal{T}_{h}^{n}} \left(\eta_{s,f,\alpha,i}^{n,m}\right)^{2}\right)^{\frac{1}{2}} + CC_{poin} \left\{\left(\sum_{E_{i}^{m} \in \mathcal{T}_{h}^{n}} \left(\eta_{t,r,\alpha,i}^{n,m}\right)^{2}\right)^{\frac{1}{2}} + \left(\sum_{E_{i}^{m} \in \mathcal{T}_{h}^{n}} \left(\eta_{s,r,\alpha,i}^{n,m}\right)^{2}\right)^{\frac{1}{2}}\right\}$$

Proof. Since s_{α}^{n} , p_{α}^{n} and $\boldsymbol{u}_{\alpha}^{n}$ are exact saturation, pressure and velocity, using the phase mass concentration formulation introduced in Section 2 to simplify the notation, for each $\psi \in X^{n}$ we have

$$\int_{J_{n}} \left(\int_{\Omega} \partial_{t} \left(\phi C_{\alpha}^{n} - \phi C_{\alpha,h,\tau}^{n} \right) \psi - \int_{\Omega} \left(\mathbf{u}_{\alpha}^{n} - \mathbf{u}_{\alpha,h,\tau}^{n} \right) \cdot \nabla \psi \right)
= \int_{J_{n}} \left(\int_{\Omega} q_{\alpha} \psi - \partial_{t} \left(\phi C_{\alpha,h,\tau}^{n} \right) \psi + \mathbf{u}_{\alpha,h,\tau}^{n} \cdot \nabla \psi \right)$$
(3.7)

We split the term $\int_{J_n} \int_{\Omega} \mathbf{u}_{\alpha,h,\tau}^n \cdot \nabla \psi$ into two parts such that

$$\int_{J_n} \int_{\Omega} \mathbf{u}_{\alpha,h,\tau}^n \cdot \nabla \psi = \int_{J_n} \int_{\Omega} \mathbf{u}_{\alpha,h}^n \cdot \nabla \psi + \int_{J_n} \sum_{\Omega_i \in \Omega} \int_{\Omega_i} \left(\mathbf{u}_{\alpha,h,\tau}^n - \mathbf{u}_{\alpha,h}^n \right) \cdot \nabla \psi$$
(3.8)

Next, we split $\int_{I_n} \int_{\Omega} \boldsymbol{u}_{\alpha,h}^n \cdot \nabla \psi$ into two parts as

$$\int_{I_n} \int_{\Omega} \boldsymbol{u}_{\alpha,h}^n \cdot \nabla \psi = -\int_{I_n} \int_{\Omega} \left(\nabla \cdot \boldsymbol{u}_{up,\alpha,h}^n \right) \psi + \int_{I_n} \int_{\Omega} \left(\boldsymbol{u}_{\alpha,h}^n - \boldsymbol{u}_{up,\alpha,h}^n \right) \cdot \nabla \psi$$
(3.9)

Therefore, by Eqn. (3.7), (3.8) and (3.9), the dual norm can be separated into three terms such that

$$\int_{I_n} \left(\int_{\Omega} \partial_t \left(\phi C_{\alpha,h}^n - \phi C_{\alpha,h,\tau}^n \right) \psi - \int_{\Omega} \left(\mathbf{u}_{\alpha,h}^n - \mathbf{u}_{\alpha,h,\tau}^n \right) \cdot \nabla \psi \right) = I_1 + I_2 + I_3$$
(3.10)

where

$$I_{1} = \sum_{E_{i}^{n} \in \mathcal{T}_{h}^{n}} \int_{E_{i}^{m}} q_{\alpha} \psi - \partial_{t} \left(\phi C_{\alpha, h, \tau}^{n} \right) \psi - \nabla \cdot \boldsymbol{u}_{up, \alpha, h}^{n} \psi$$

$$(3.11)$$

$$I_{2} = \sum_{E_{i}^{m} \in \mathcal{T}_{h}^{n}} \int_{E_{i}^{m}} \left(\boldsymbol{u}_{\alpha,h}^{n} - \boldsymbol{u}_{up,\alpha,h}^{n} \right) \cdot \nabla \psi$$
(3.12)

$$I_{3} = \sum_{E_{i}^{n} \in \mathcal{T}_{h}^{n} E_{i}^{m}} \int \left(\mathbf{u}_{\alpha,h,\tau}^{n} - \mathbf{u}_{\alpha,h}^{n} \right) \cdot \nabla \psi$$
(3.13)

Since $s_{\alpha,h}^n$, $p_{\alpha,h}^n$, $u_{\alpha,h}^n$ are the numerical solutions of Eqn. (2.9) and (2.10) we have the following

$$\sum_{E_i^m \in \mathcal{T}_h^n E_i^m} \int \left(q_{\alpha} - \partial_t \left(\phi C_{\alpha, h, \tau}^n \right) - \nabla \cdot \boldsymbol{u}_{up, \alpha, h}^n \right) w = 0 \quad \forall w \in W_h^n$$
(3.14)

We take $w = \prod_{W_{i}^{n}} \psi$ and by Poincaré inequality obtain the following bound for I_{1}

$$I_{1} = \sum_{E_{i}^{m} \in \mathcal{T}_{h}^{n}} \int_{E_{i}^{m}} \left(q_{\alpha} - \partial_{t} \left(\phi C_{\alpha,h,\tau}^{n} \right) - \nabla \cdot \boldsymbol{u}_{up,\alpha,h}^{n} \right) \left(\psi - \Pi_{W_{h}^{n}} \psi \right)$$

$$\leq C_{poin} \sum_{E_{i}^{m} \in \mathcal{T}_{h}^{n}} \left(\eta_{t,r,\alpha,i}^{n,m} + \eta_{s,r,\alpha,i}^{n,m} \right) \left(\| \nabla \psi \|_{L^{2}(E_{i}^{m})} + \| \psi_{t} \|_{L^{2}(E_{i}^{m})} \right)$$

$$\leq CC_{poin} \left\{ \left(\sum_{E_{i}^{m} \in \mathcal{T}_{h}^{n}} \left(\eta_{s,r,\alpha,i}^{n,m} \right)^{2} \right)^{\frac{1}{2}} + \left(\sum_{E_{i}^{m} \in \mathcal{T}_{h}^{n}} \left(\eta_{t,r,\alpha,i}^{n,m} \right)^{2} \right)^{\frac{1}{2}} \right\} \| \psi \|_{X^{n}}$$

$$(3.15)$$

Next for I_2 , by Cauchy-Schwarz inequality we have

$$I_{2} = \sum_{E_{i}^{m} \in \mathcal{T}_{h}^{n}} \int_{E_{i}^{m}} \left(\boldsymbol{u}_{\alpha,h}^{n} - \boldsymbol{u}_{up,\alpha,h}^{n} \right) \cdot \nabla \psi \leq \sum_{E_{i}^{m} \in \mathcal{T}_{h}^{n}} \eta_{s,f,\alpha,i}^{n,m} \| K^{\frac{1}{2}} \nabla \psi \|_{L^{2}(E_{i}^{m})} \leq \left(\sum_{E_{i}^{m} \in \mathcal{T}_{h}^{n}} \left(\eta_{s,f,\alpha,i}^{n,m} \right)^{2} \right)^{\frac{1}{2}} \| \psi \|_{X^{n}}$$

$$(3.16)$$

Similarly, I3 goes as

$$I_{3} = \sum_{E_{i}^{m} \in \mathcal{T}_{h}^{n}} \int_{E^{m}} \left(\mathbf{u}_{\alpha,h,\tau}^{n} - \mathbf{u}_{\alpha,h}^{n} \right) \cdot \nabla \psi \leq \left(\sum_{E_{i}^{m} \in \mathcal{T}_{h}^{n}} \left(\eta_{t,f,\alpha,i}^{n,m} \right)^{2} \right)^{\frac{1}{2}} \|\psi\|_{X^{n}}$$

$$(3.17)$$

By the definition of N_{α} , the inequality for the dual norm of the residual is proved. \Box

In the following lemma, we will provide an upper bound estimate for the non-nonconformity error measure.

Lemma 3. Assuming $K \in C^1(\Omega)$, there exist constant C such that

$$N_{\alpha,p}^{n} \leq C \left\{ \left(\sum_{E_{i}^{m} \in \mathcal{T}_{h}^{n}} \left(\eta_{t,p,\alpha,i}^{n,m} \right)^{2} \right)^{\frac{1}{2}} + \left(\sum_{E_{i}^{m} \in \mathcal{T}_{h}^{n}} \left(\eta_{s,p,\alpha,i}^{n,m} \right)^{2} \right)^{\frac{1}{2}} \right\}$$

Proof. First, using Helmholtz decomposition, we have

$$K^{-1}\tilde{\boldsymbol{u}}_{\alpha,h,\tau}^{n} = \nabla\phi_0 + \nabla \times \phi_1 \tag{3.18}$$

with $\phi_0 \in H^1(\Omega)$, $\phi_1 \in H(curl, \Omega)$ for d = 3 and $\phi_1 \in H^1(\Omega)$ for d = 2. Since $\psi \in X^n$, $\nabla \psi \in L^2(J_n \times \Omega)$. Meanwhile $\nabla \phi_0 \in L^2(\Omega)$ thus we have

$$\inf_{\psi \in X^n} \int_{J_n} \int_{\Omega} K^{-1} \left| \tilde{u}_{\alpha,h,\tau}^n + K \nabla \psi \right|^2 \le \int_{J_n} \int_{\Omega} K^{-1} \left| \tilde{u}_{\alpha,h,\tau}^n - K \nabla \phi_0 \right|^2 \tag{3.19}$$

We will estimate the term $\int_{I_n} \int_{\Omega} K^{-1} |\tilde{u}_{\alpha,h}^n - K \nabla \phi_0|^2$. By Eqn. (3.18), we have

$$\int_{J_n} \int_{\Omega} K^{-1} \left| \tilde{u}_{\alpha,h,\tau}^n - K \nabla \phi_0 \right|^2 = \int_{J_n} \int_{\Omega} K \left| \nabla \times \phi_1 \right|^2. \tag{3.20}$$

By Eqn. (3.18) and $\nabla \phi_0 \perp \nabla \times \phi_1$, we have

$$\int_{J_n} \int_{\Omega} |\nabla \times \phi_1|^2 = \int_{J_n} \int_{\Omega} \left(K^{-1} \tilde{\mathbf{u}}_{\alpha,h}^n - \nabla \phi_0 \right) \cdot \left(\nabla \times \phi_1 \right)
= \int_{J_n} \int_{\Omega} \left(K^{-1} \tilde{\mathbf{u}}_{\alpha,h}^n \right) \cdot \left(\nabla \times \phi_1 \right) \tag{3.21}$$

Using Lemma 1 and the Trace Theorem, there exist a $\Pi_{M_h^{n,*}}\phi_1\in M_h^{n,*}$ such that for all $E_i^m\in\mathcal{T}_h^n$,

$$\begin{split} \sum_{E_i^m \in \mathcal{T}_h^n} \left| E_i^m \right|^{-2} \left\| \phi_1 - \Pi_{M_h^{n,*}} \phi_1 \right\|_{L^2(E_i^m)}^2 &\leq C \Big(\left\| \nabla \phi_1 \right\|_{L^2(J_n; L^2(\Omega))}^2 + \left\| \partial_t \phi_1 \right\|_{L^2(J_n; L^2(\Omega))}^2 \Big) \\ & \sum_{e \in \mathcal{E}^n} |e|^{-1} \left\| \phi_1 - \Pi_{M_h^{n,*}} \phi_1 \right\|_{L^2(e)}^2 &\leq C \Big(\left\| \nabla \phi_1 \right\|_{L^2(J_n; L^2(\Omega))}^2 + \left\| \partial_t \phi_1 \right\|_{L^2(J_n; L^2(\Omega))}^2 \Big). \end{split}$$

Also $\nabla \times \Pi_{M_h^{n,*}} \phi_1 \in V_h^{n,*}$, by Eqn. (2.10) we have

$$\int_{I_n} \int_{\Omega} K^{-1} \tilde{\boldsymbol{u}}_{\alpha,h}^n \cdot \left(\nabla \times \Pi_{M_h^{n,*}} \phi_1 \right) = \int_{I_n} \int_{\Omega} p_{\alpha,h}^n \nabla \cdot \left(\nabla \times \Pi_{M_h^{n,*}} \phi_1 \right) = 0$$

Therefore, we have

$$\int_{J_{n}} \int_{\Omega} \left(K^{-1} \tilde{\boldsymbol{u}}_{\alpha,h}^{n} \right) \cdot \left(\nabla \times \phi_{1} \right) \\
= \int_{J_{n}} \int_{\Omega} \left(K^{-1} \tilde{\boldsymbol{u}}_{\alpha,h}^{n} \right) \cdot \left[\nabla \times \left(\phi_{1} - \Pi_{M_{h}^{n,*}} \phi_{1} \right) \right] \\
\leq \int_{J_{n}} \int_{\Omega} \nabla \times \left(K^{-1} \tilde{\boldsymbol{u}}_{\alpha,h}^{n} \right) \cdot \left(\phi_{1} - \Pi_{M_{h}^{n,*}} \phi_{1} \right) + \sum_{e \in \mathcal{E}_{h}^{n}} \int_{J_{n}} \int_{e} \left[\left(K^{-1} \tilde{\boldsymbol{u}}_{\alpha,h}^{n} \right) \times \boldsymbol{n} \right] \cdot \left(\phi_{1} - \Pi_{M_{h}^{n,*}} \phi_{1} \right) \\
\leq \sum_{E_{i}^{m} \in \mathcal{T}_{h}^{n}} \left\| \nabla \times \left(K^{-1} \tilde{\boldsymbol{u}}_{\alpha,h}^{n} \right) \right\|_{L^{2}(E_{i}^{m})} \left\| \phi_{1} - \Pi_{M_{h}^{n,*}} \phi_{1} \right\|_{L^{2}(E_{i}^{m})} + \sum_{e \in \mathcal{E}_{h}^{n}} \left\| \left(K^{-1} \tilde{\boldsymbol{u}}_{\alpha,h}^{n} \right) \times \boldsymbol{n} \right\|_{L^{2}(e)} \left\| \phi_{1} - \Pi_{M_{h}^{n,*}} \phi_{1} \right\|_{L^{2}(e)} \\$$

Apply Eqn. (3.22) to Eqn. (3.21) we obtain

$$\int_{J_{n}} \int_{\Omega} |\nabla \times \phi_{1}|^{2} \leq C \left(\sum_{E_{i}^{m} \in \mathcal{T}_{h}^{n}} |E_{i}^{m}|^{2} \|\nabla \times \left(K^{-1} \tilde{\boldsymbol{u}}_{\alpha,h,\tau}^{n}\right)\|_{L^{2}(E_{i}^{m})}^{2} \right)^{\frac{1}{2}} \left(\|\nabla \phi_{1}\|_{L^{2}(J_{n};L^{2}(\Omega))}^{2} + \|\partial_{t} \phi_{1}\|_{L^{2}(J_{n};L^{2}(\Omega))}^{2} \right)^{\frac{1}{2}} \\
+ C \left(\sum_{e \in \mathcal{E}_{h}^{n}} |e| \|\left(K^{-1} \tilde{\boldsymbol{u}}_{\alpha,h,\tau}^{n}\right) \times \boldsymbol{n}\|_{L^{2}(e)}^{2} \right)^{\frac{1}{2}} \left(\|\nabla \phi_{1}\|_{L^{2}(J_{n};L^{2}(\Omega))}^{2} + \|\partial_{t} \phi_{1}\|_{L^{2}(J_{n};L^{2}(\Omega))}^{2} \right)^{\frac{1}{2}} \\
\leq C \left(\sum_{E_{i}^{m} \in \mathcal{T}_{h}^{n}} \left(\eta_{s,p,\alpha,i}^{n,m}\right)^{2} \right)^{\frac{1}{2}} \left(\|\nabla \phi_{1}\|_{L^{2}(J_{n};L^{2}(\Omega))}^{2} + \|\partial_{t} \phi_{1}\|_{L^{2}(J_{n};L^{2}(\Omega))}^{2} \right)^{\frac{1}{2}} \right)$$
(3.23)

Next, we establish inequality for $\left\|
abla \phi_1
ight\|_{L^2(J_n;L^2(\Omega))}^2$ with

$$\|\nabla\phi_1\|_{L^2(J_n;L^2(\Omega))}^2 = \|\nabla\times\phi_1\|_{L^2(J_n;L^2(\Omega))}^2 \le \|\nabla\times\phi_1\|_{L^2(J_n;L^2(\Omega))}^2$$
(3.24)

Using (3.24), we have

$$\int_{J_{n}} \int_{\Omega} \left| \nabla \times \phi_{1} \right|^{2} \leq C \left(\sum_{E_{i}^{m} \in \mathcal{T}_{h}^{n}} \left(\eta_{s,p,\alpha,i}^{n,m} \right)^{2} \right)^{\frac{1}{2}} \left(\left\| \nabla \phi_{1} \right\|_{L^{2}(J_{n};L^{2}(\Omega))}^{2} + \left\| \partial_{t} \phi_{1} \right\|_{L^{2}(J_{n};L^{2}(\Omega))}^{2} \right)^{\frac{1}{2}} \\
\leq C \left\{ \sum_{E_{i}^{m} \in \mathcal{T}_{h}^{n}} \left(\eta_{s,p,\alpha,i}^{n,m} \right)^{2} + \left(\left\| \nabla \phi_{1} \right\|_{L^{2}(J_{n};L^{2}(\Omega))}^{2} + \left\| \partial_{t} \phi_{1} \right\|_{L^{2}(J_{n};L^{2}(\Omega))}^{2} \right) \right\} \\
\leq C \left\{ \sum_{E_{i}^{m} \in \mathcal{T}_{h}^{n}} \left(\eta_{s,p,\alpha,i}^{n,m} \right)^{2} + \left\| \partial_{t} \phi_{1} \right\|_{L^{2}(J_{n};L^{2}(\Omega))}^{2} \right\} \tag{3.25}$$

Also for $\|\partial_t \phi_1\|_{L^2(J_n;L^2(\Omega))}^2$,

$$\|\partial_{t}\phi_{1}\|_{L^{2}(J_{n};L^{2}(\Omega))}^{2} \leq \|\partial_{t}\phi_{1}\|_{L^{2}(J_{n};L^{2}(\Omega))}^{2} + \|\partial_{t}\phi_{0}\|_{L^{2}(J_{n};L^{2}(\Omega))}^{2}$$

$$\leq \|K^{-1}\partial_{t}\tilde{u}_{\alpha,h,\tau}^{n}\|_{L^{2}(J_{n};L^{2}(\Omega))}^{2} \leq C \sum_{E_{t}^{m}\in\mathcal{T}_{t}^{n}} \left(\eta_{t,p,\alpha,i}^{n,m}\right)^{2}$$
(3.26)

Then the nonconformity error measure is bounded by

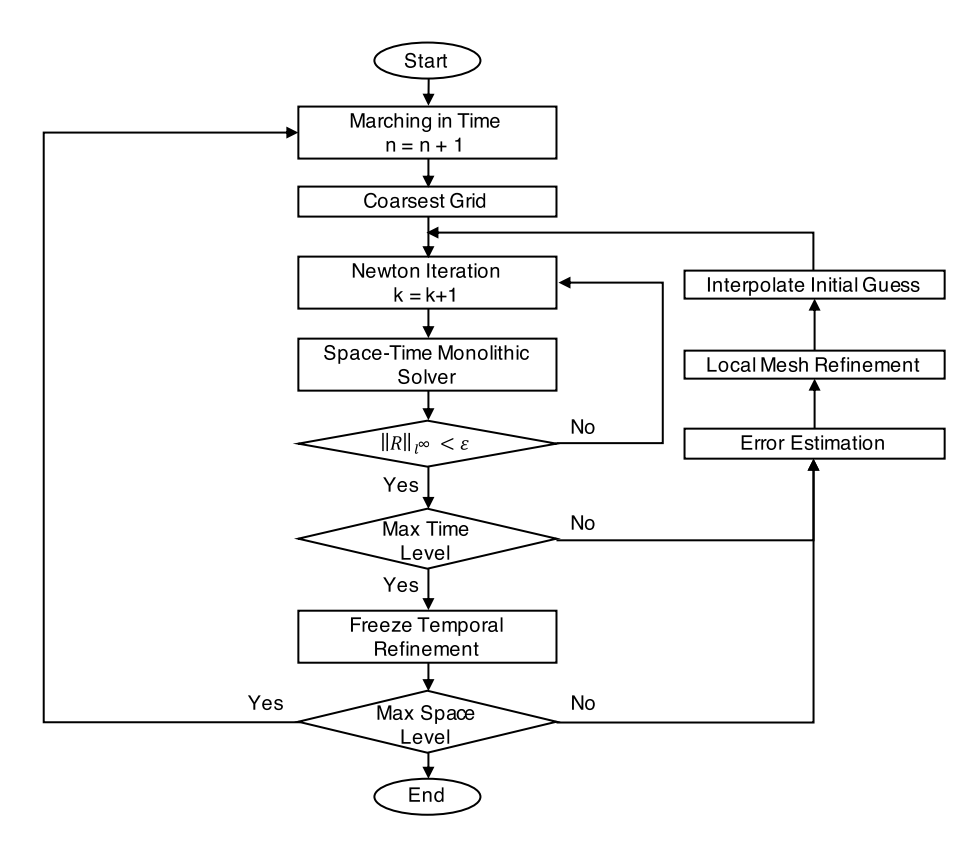


Fig. 2. Solution algorithm for sequential local mesh refinement solver with separate temporal and spatial adaptivity.

$$N_{\alpha,p}^{n} = \inf_{\psi \in X^{n}} \left\{ \int_{J_{n}} \int_{\Omega} K^{-1} \left(\tilde{\boldsymbol{u}}_{\alpha,h,\tau}^{n} + K \nabla \psi \right)^{2} \right\}^{\frac{1}{2}}$$

$$\leq \left\{ \int_{J_{n}} \int_{\Omega} K \left| \nabla \times \phi_{1} \right|^{2} \right\}^{\frac{1}{2}}$$

$$\leq C \left\{ \left(\sum_{E_{i}^{m} \in \mathcal{T}_{h}^{n}} \left(\eta_{s,p,\alpha,i}^{n,m} \right)^{2} \right)^{\frac{1}{2}} + \left(\sum_{E_{i}^{m} \in \mathcal{T}_{h}^{n}} \left(\eta_{t,p,\alpha,i}^{n,m} \right)^{2} \right)^{\frac{1}{2}} \right\}$$

$$(3.27)$$

The inequality of the nonconformity error measure is proved. \Box

The error estimator introduced in this section is used to search for refinement regions. In the next section, we will introduce our sequential local mesh refinement algorithm to reduce the size of the system and minimize the number of iterations required for convergence, while maintaining accuracy as compared to uniformly fine scale solution.

4. Solution algorithm

In this section we present the sequential local mesh refinement solver algorithm. The procedure starts by solving the problem at its coarsest resolution in space-time domain and then sequentially refines certain regions to its finest resolution. The coarsest time step is chosen such that the numerical convergence is guaranteed on the coarsest spatial grid. During the sequential refinement process, the solver first keeps the spatial mesh static at its coarsest level and searches for regions to refine in time. Once the last level of temporal refinement is implemented, the temporal discretization is finalized and the solver refines the mesh in space until reaching the finest resolution. Then the spatial grid is restored to the coarsest resolution, the solver marches forward in time with the coarsest time step and the whole process reiterates. The complete algorithm is illustrated in Fig. 2. We always start from the coarsest mesh and refines into deeper levels due to the tree data structure inherited from [15,18,30]. The tree structure is represented by a group of pointers linked to each other. Allowing both refinement and agglomeration requires inserting and removing pointers in the middle of the tree and then

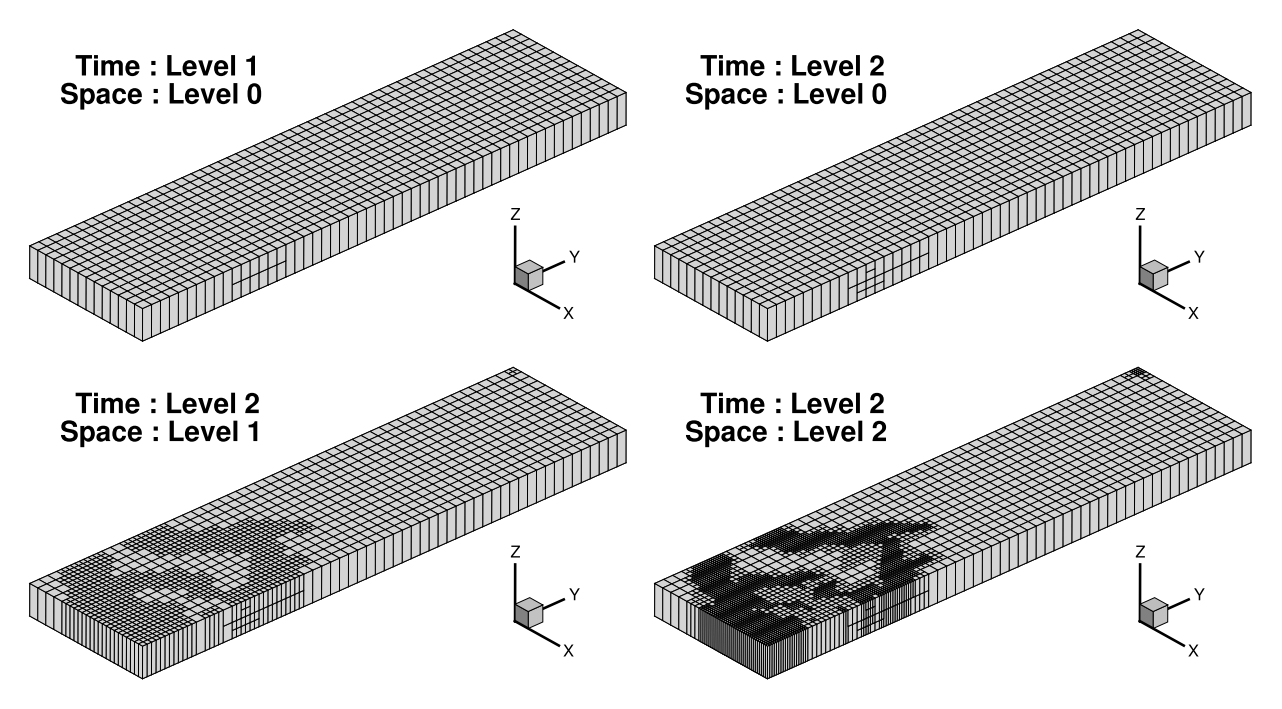


Fig. 3. Sample grid generated during sequential local mesh refinement from coarsest to finest space-time resolution.

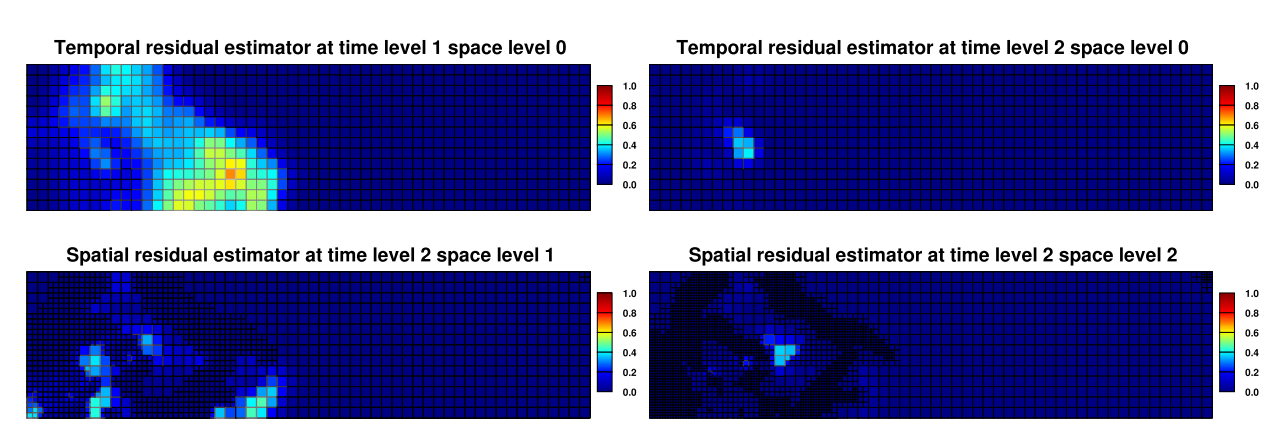


Fig. 4. Normalized spatial and temporal residual estimator at each space and time refinement level.

re-associating hanging pointers. The toll caused by such complex operation will counteract the computational efficiency improvement. By constraining the operation to solely refinement, we are only required to evolve the tree by adding new levels on the bottom, which has a much smaller operation count.

Fig. 3 demonstrates a sample semi-structured grid generated with the algorithm stated above. Here the *z* axis represents time in a 2-D spatial problem. Separating temporal and spatial refinement makes the mesh construction more flexible. As observed from the plot, subdomains can have temporal refinement, spatial refinement or both. This flexibility reduces the total number of elements by two to three times as compared to the isotropic refinement scheme implemented in [30], thus improving computational performance. Note that the solver always refine spatially to the finest resolution for cells with well contained, for accurate estimate of production rate and bottom-hole flowing pressure. Adding temporal refinements for these cells depends on whether the saturation front is sweeping through the well or not.

We use the error estimators defined in Section 3 to scan regions for refinement that in return diminishes the upper bound of the error measure. First we study the temporal and spatial residual estimators defined by Eqn. (3.1) and (3.2), similar to [34]. Provided by linear projection of the solution on the previous mesh, the initial guess of unknowns after each refinement procedure is naturally close to the true solution. Consequently, the residual estimators is only useful for indicating the main refinement region on the coarsest space-time resolution. Large estimator values appears only sporadically on all other resolutions as demonstrated by Fig. 4. The sporadic appearance infers strong heterogeneity of the underlying petrophysical properties.

The most important estimators to ensure solution convergence and accuracy are the flux estimators. Let us first review the temporal one represented by Eqn. (3.3). We expand the original formulation as the following.

$$\eta_{t,f,\alpha,i}^{n,m} = \left\{ \int\limits_{E_i^m} K^{-1} \left| \frac{\mathbf{u}_{\alpha,h}|_{\tau_{i,1}^m} - \mathbf{u}_{\alpha,h}|_{\tau_{i,0}^m}}{\tau_{i,1}^m - \tau_{i,0}^m} (\tau_{i,1}^m - t) \right| \right\}^{\frac{1}{2}} = \left\{ \left| F_i^m \left| K^{-1} \left| \mathbf{u}_{\alpha,h} \right|_{\tau_{i,1}^m} - \mathbf{u}_{\alpha,h} \right|_{\tau_{i,0}^m} \right|^2 \frac{\tau_{i,1}^m - \tau_{i,0}^m}{3} \right\}^{\frac{1}{2}}$$

Then the output is mainly controlled by the temporal flux difference term $\mathbf{u}_{\alpha,h}|_{\tau_{i,1}^m} - \mathbf{u}_{\alpha,h}|_{\tau_{i,0}^m}$, which we can further expand to

$$\begin{aligned} \mathbf{u}_{\alpha,h}|_{\tau_{i,1}^{m}} - \mathbf{u}_{\alpha,h}|_{\tau_{i,0}^{m}} &= -\frac{K}{\mu_{\alpha}} \rho_{\alpha} \left(p_{\alpha,h}|_{\tau_{i,1}^{m}} \right) \nabla p_{\alpha,h}|_{\tau_{i,1}^{m}} \left\{ k_{r\alpha} \left(s_{\alpha,h}|_{\tau_{i,1}^{m}} \right) - k_{r\alpha} \left(s_{\alpha,h}|_{\tau_{i,0}^{m}} \right) \right\} \\ &- \frac{K}{\mu_{\alpha}} k_{r\alpha} \left(s_{\alpha,h}|_{\tau_{i,0}^{m}} \right) \left\{ \rho_{\alpha} \left(p_{\alpha,h}|_{\tau_{i,1}^{m}} \right) \nabla p_{\alpha,h}|_{\tau_{i,1}^{m}} - \rho_{\alpha} \left(p_{\alpha,h}|_{\tau_{i,0}^{m}} \right) \nabla p_{\alpha,h}|_{\tau_{i,0}^{m}} \right\} \end{aligned}$$

The second term in the above equation is effectively zero in slightly compressible flow since density variation caused by pressure is negligible and pressure gradient stays fairly constant in time. Moreover, temporal refinement is not necessary if large estimator output is caused by the leading constant $\frac{K}{\mu_{\alpha}}\rho_{\alpha}(p_{\alpha,h}|_{\tau_{i,1}^m})\nabla p_{\alpha,h}|_{\tau_{i,1}^m}$ in the first term (for example regions around the well with large pressure gradient), since pressure solution is smooth in time and does not trigger any convergence issues. We need to apply temporal refinement in regions with large $\eta_{t,f,\alpha,i}^{n,m}$ caused specifically by significant change in relative permeability $k_{r\alpha}(s_{\alpha,h}|_{\tau_{i,1}^m}) - k_{r\alpha}(s_{\alpha,h}|_{\tau_{i,0}^m})$. Therefore we calculate the temporal water saturation gradient

$$\varepsilon_{t,w,i}^{n,m} = \left| \frac{\partial}{\partial t} s_{w,h,i}^{n,m} \right| \tag{4.1}$$

and applied refinement exclusively to regions with both $\eta^{n,m}_{t,f,\alpha,i}$ and $\varepsilon^{n,m}_{t,w,i}$ values exceeding the threshold. Similarly, the spatial flux estimator $\eta^{n,m}_{s,f,\alpha,i}$ in Eqn. (3.4) can be expanded to

$$\eta_{s,f,\alpha,i}^{n,m} = \left\{ \left| F_i^m \right| \left| \tau_{i,1}^m - \tau_{i,0}^m \right| K^{-1} \left| \mathbf{u}_{up,\alpha,h} - \mathbf{u}_{\alpha,h} \right|^2 \right\}^{\frac{1}{2}}$$

with the output mainly controlled by the flux spatial difference $u_{up,\alpha,h} - u_{\alpha,h}$. We can also expand this term as the following.

$$\mathbf{u}_{up,\alpha,h} - \mathbf{u}_{\alpha,h} = -K \rho_{\alpha} \frac{k_{r\alpha}(s_{up,\alpha,h}) - k_{r\alpha}(s_{\alpha,h})}{\mu_{\alpha}} \nabla p_{\alpha,h}$$

Surely, we need to refine regions with significant change in relative permeability $k_{r\alpha}(s_{up,\alpha,h}) - k_{r\alpha}(s_{\alpha,h})$ to accurately represent the features of the reservoir. Furthermore regions with large estimator output caused by the leading constant $\frac{K}{\mu_{\alpha}}\rho_{\alpha}\nabla p_{\alpha,h}$ also need special care. Such regions are characterized by rapid mass flow and refining them facilitates convergence. Therefore we calculate the spatial water saturation gradient.

$$\varepsilon_{s,w,i}^{n,m} = \begin{cases} \left\| \nabla s_{w,h,i}^{n,m}(\boldsymbol{x}) \right\|_{l^{\infty}} & \text{if } \left\| \nabla s_{w,h,i}^{n,m}(\boldsymbol{x}) \right\|_{l^{\infty}} > \left\| \nabla s_{w,h,i}^{n-1,m}(\boldsymbol{x}) \right\|_{l^{\infty}} \\ \frac{1}{2} \left(\left\| \nabla s_{w,h,i}^{n,m}(\boldsymbol{x}) \right\|_{l^{\infty}} + \left\| \nabla s_{w,h,i}^{n-1,m}(\boldsymbol{x}) \right\|_{l^{\infty}} \right) & \text{if } \left\| \nabla s_{w,h,i}^{n,m}(\boldsymbol{x}) \right\|_{l^{\infty}} \le \left\| \nabla s_{w,h,i}^{n-1,m}(\boldsymbol{x}) \right\|_{l^{\infty}} \end{cases}$$

$$(4.2)$$

and apply refinement to regions with either $\eta_{s,f,\alpha,i}^{n,m}$ or $\varepsilon_{s,w,i}^{n,m}$ values exceeding the threshold. Please note that we are taking some extra steps when calculating spatial saturation gradient by looking at the previous time step values. This mechanism ensures a more accurate exposure of features in the system, especially in channelized permeability distributions. Fig. 5 and 6 show flux estimator and saturation gradient at each refinement level.

Instead of setting a subjective threshold, we outline the regions for refinement by distribution percentiles. We first define [0.01, 1] as the analysis range of flux error estimator and saturation gradient. Values below 0.01 are considered too small and thus neglected. The threshold is determined by distribution. The cumulative distribution function of flux error estimator and saturation gradient at each refinement level is plotted in Fig. 7 against sample data collected during simulation. As illustrated by the graphs, the data for both variables generally follow log-normal distribution trend. During temporal adaptation, we refine cells with 50% largest values in both flux estimator and saturation gradient. Therefore, we use the log-mean, which covers approximately 50% of the analysis range, as the threshold. We notice that during temporal refinement, the cumulative distribution functions of both variables are better described by normal distribution. However, we still choose the log-mean as the threshold since it leads to a slight over-refinement in time and thus better guarantees Newton convergence. During spatial adaptation, we refine cells with either 50% largest values in the saturation gradient

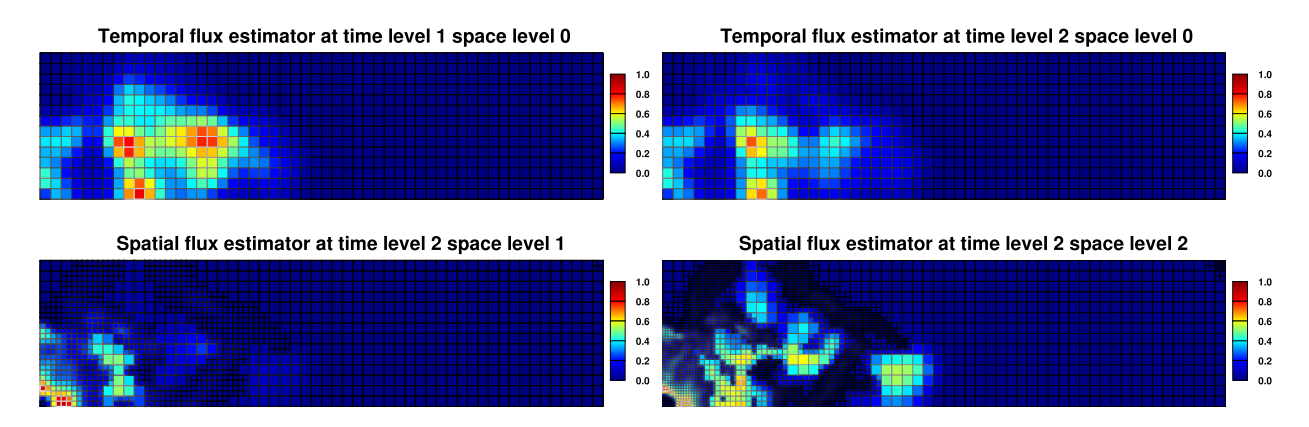


Fig. 5. Normalized flux estimator at each space and time refinement level.

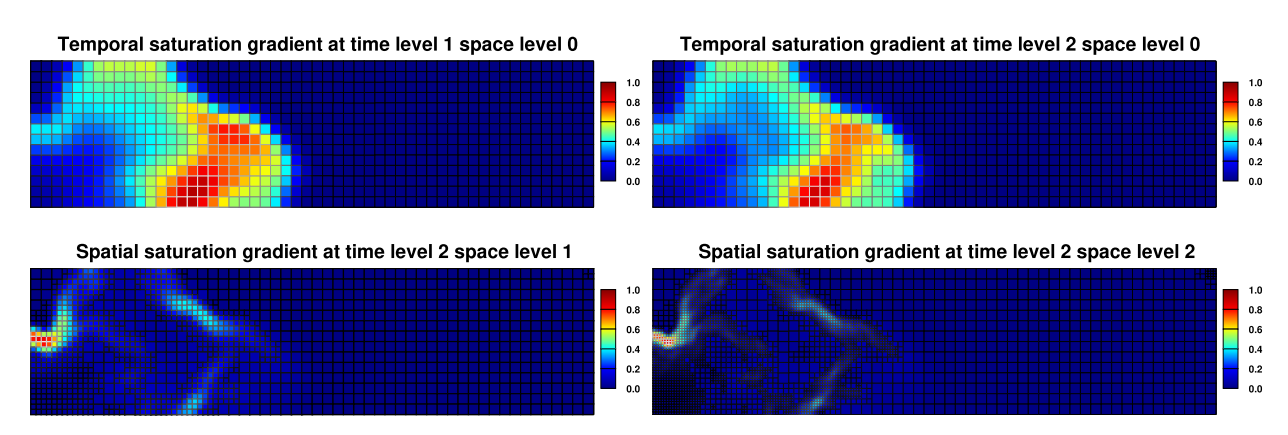


Fig. 6. Normalized saturation gradient at each space and time refinement level.

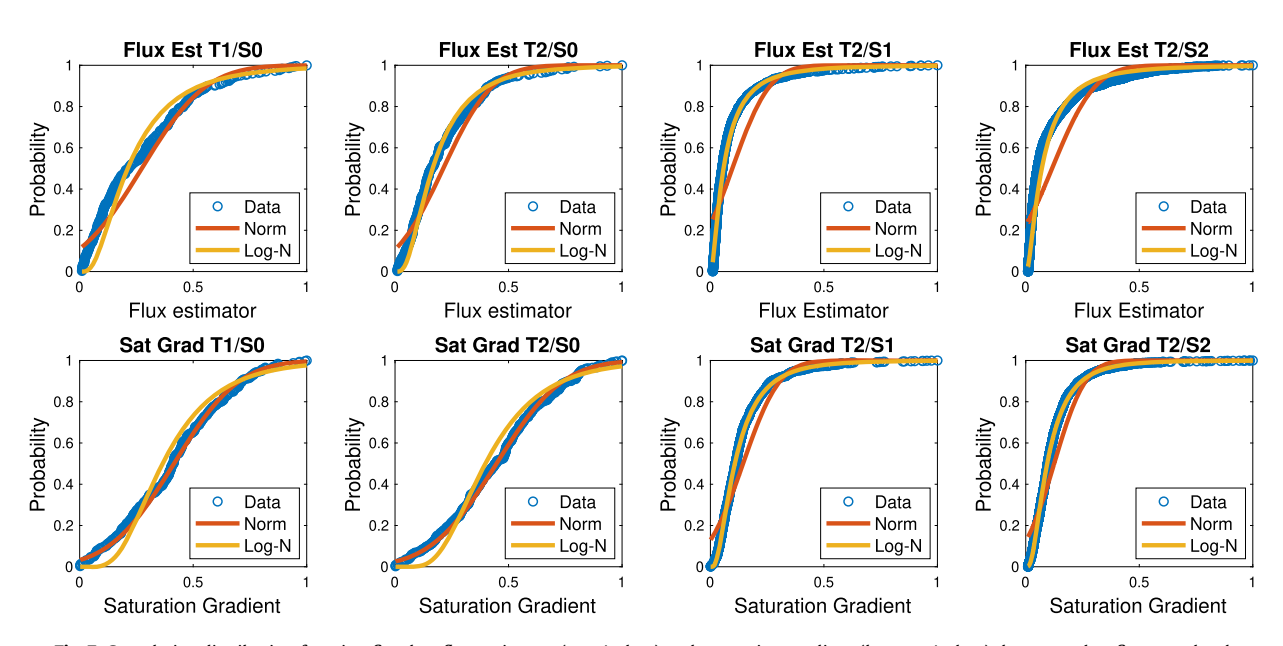


Fig. 7. Cumulative distribution function fitted to flux estimator (top 4 plots) and saturation gradient (bottom 4 plots) data at each refinement level.

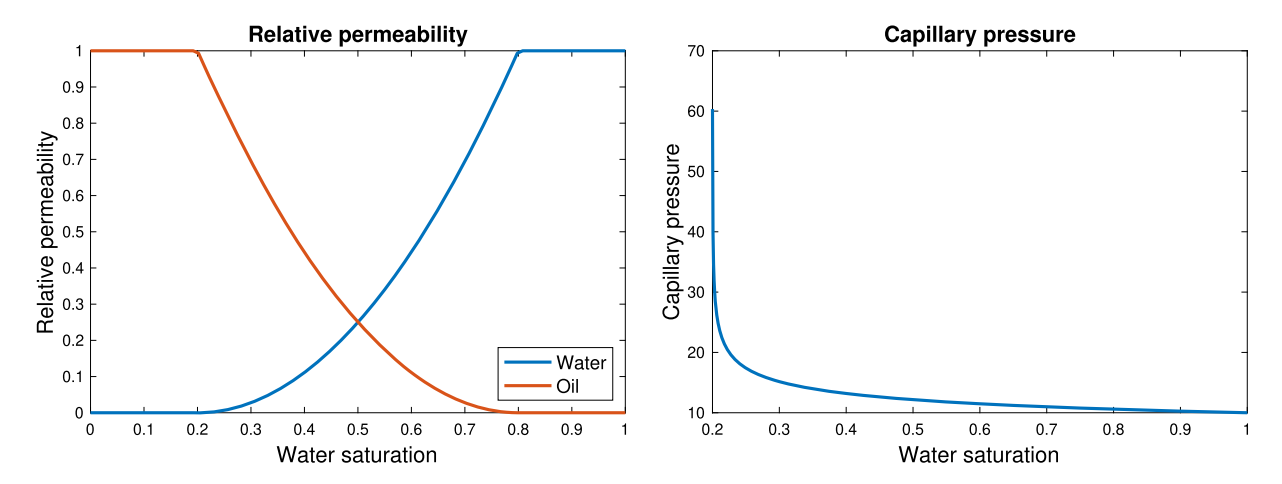


Fig. 8. Relative permeability (left) and capillary pressure (right) curve for numerical experiments.

or 10% largest values in flux estimator. Therefore, the thresholds for the two variables are the log-mean and one standard deviation above the log-mean, corresponding to their respective distribution.

Finally for the non-conformity estimators, $\eta_{t,p,\alpha,i}^{n,m}$ is naturally diminished during temporal refinement using $\eta_{t,f,\alpha,i}^{n,m}$ since the two estimators have similar formulations. $\eta_{s,p,\alpha,i}^{n,m}$ represents the tangential gradient of flux on non-conformal grid interfaces. To reduce this term, we apply mesh smoothing algorithm. Adjacent grid cells cannot be more than one refinement level apart within the hierarchical tree structure in both spatial and temporal dimensions. Such algorithm also ensures a smooth transition from fine grid into coarse grid and thus facilitates convergence.

5. Numerical results

In this section we will first show results from two numerical experiments on 2-D slightly compressible two-phase flow model. Both experiments use the same fluid data from the SPE10 dataset [9]. The oil and water reference densities in Eqn. (2.5) are taken to be 53 lb/ft³ and 64 lb/ft³ and compressibilities are 1×10^{-4} psi⁻¹ and 3×10^{-6} psi⁻¹ respectively. The fluid viscosity is 3 and 1 [cp] for oil and water phase. We use Brooks's Corey model for both relative permeability and capillary pressure. The equations for relative permeability are

$$\begin{cases} k_{rw} = k_{rw}^{0} \left(\frac{s_{w} - s_{wirr}}{1 - s_{or} - s_{wirr}} \right)^{n_{w}} \\ k_{ro} = k_{ro}^{0} \left(\frac{s_{o} - s_{or}}{1 - s_{or} - s_{wirr}} \right)^{n_{o}} \end{cases}$$
(5.1)

The endpoint values are $s_{or} = s_{wirr} = 0.2$ and $k_{ro}^0 = k_{rw}^0 = 1.0$ while the model exponents are $n_w = n_0 = 2$. The equation for capillary pressure is

$$p_c(s_w) = P_{en,cow} \left(\frac{1 - s_{wirr}}{s_w - s_{wirr}} \right)^{l_{cow}}$$
(5.2)

with $P_{en,cow} = 10$ psi and $l_{cow} = 0.2$. Fig. 8 visualizes the relative permeability and capillary pressure curve. The two experiments use Gaussian-like and channelized permeability and porosity distributions from SPE 10 dataset [9] layer 20 and 52, respectively. The reservoir size is 56 ft × 216 ft × 1 ft. We place a water rate specified injection well at the bottom left corner and a pressure specified production well at the upper right corner. The water injection rate is 1 ft³/day and production pressure is 1000 psi. Furthermore, the initial pressure and water saturation are set to be 1000 psi and 0.2.

5.1. Gaussian-like permeability distribution

The Gaussian-like permeability field comes from SPE 10 dataset layer 20. The fine scale petrophysical data are shown in Fig. 9, assuming isotropic permeability. We allow three refinement levels in both space and time in our experiment. Although the framework allows different refinement ratios between levels, for the sake of simplicity we set the same ratio, a factor of 2, between all levels. We use the numerical homogenization technique introduced in [4] to upscale the fine scale permeability to different coarse levels. This calculation only needs to be performed once at the beginning of the experiment. The homogenized permeability distribution in *X* and *Y* directions, which does not manifest high anisotropy, is illustrated in

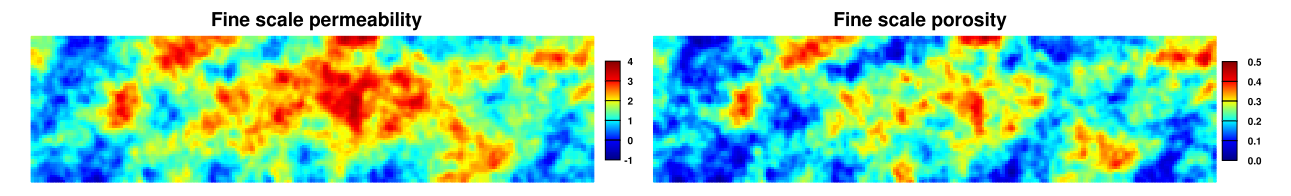


Fig. 9. Gaussian-like fine scale permeability (left) and porosity (right) distribution.

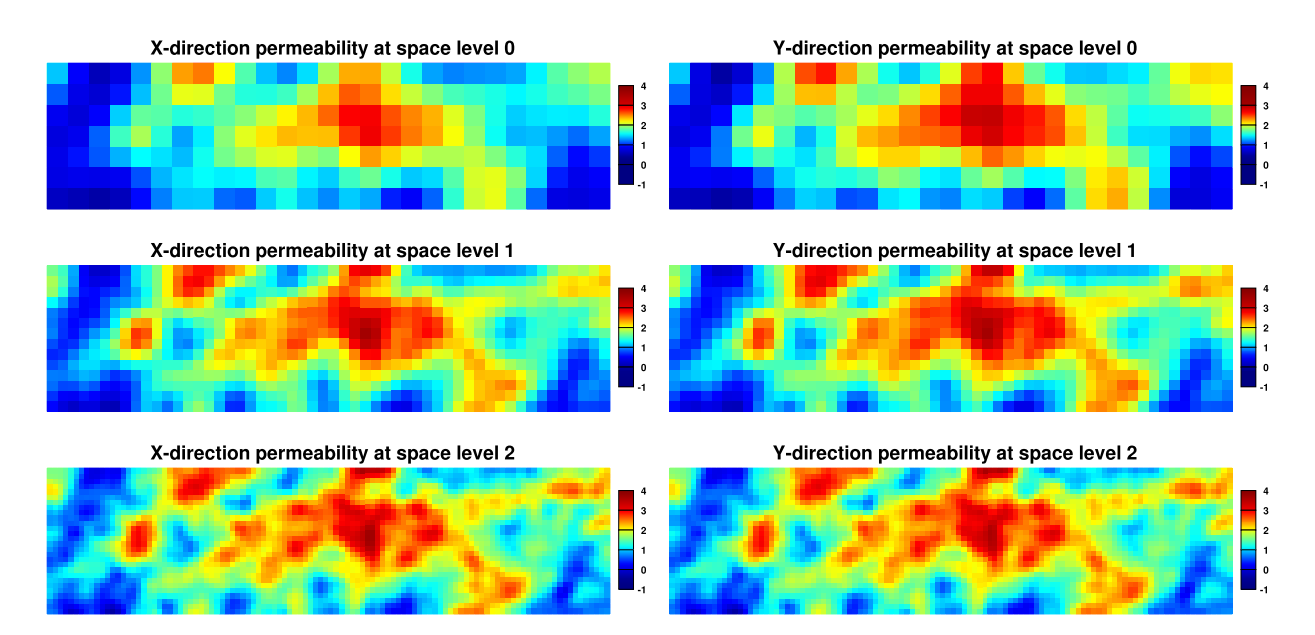


Fig. 10. Homogenized Gaussian-like permeability in X and Y direction for each space level.

Fig. 10. The porosity is upscaled simply by weighted volumetric average and therefore is not visualized. The computational domain is 56 ft \times 216 ft \times 1 ft \times 1000 days with coarsest and finest element size of 8 ft \times 8 ft \times 1 ft \times 10 days and 1 ft \times 1 ft \times 1 ft \times 1.25 days.

The adaptive water saturation profile with its mesh as compared to fine scale solution at 100 and 500 days are plotted in Fig. 11. We observe the finest mesh stays concentrated at the water front to correctly capture the dramatic changes in saturation. In this region, mass transfer is not dominated by either oil or water phase and thus contributes the most non-linearity and requires temporal refinement for stable Newton convergence. Elements behind the water front is gradually coarsened due to the decreased saturation variation. Overall, the saturation profile provided by the sequential refinement solver looks similar to the fine scale solution. Fig. 12 shows the production rates and cumulative recoveries of the two solutions, which are nearly identical. The oil rate from the sequential refinement solver appears to be slightly smoother at the early time which is caused by the coarse mesh.

The program execution time is presented in Fig. 13. The total execution time consists of system setup which constructs the linear system, solving the linear system and data handle which mainly involves copying and pasting data from the current to the previous time step. Since the experiment problem size is still small, we use both direct and iterative solver to resolve the linear system. The semi-structured space-time mesh results in highly non-symmetric matrices and therefore we use GMRES with ILU preconditioner as our iterative solver. We observe 8 and 4 times speedup on system setup and data handle using direct solver. These two types of operations are strongly dependent upon the number of time steps taken and total number of refinement levels. Hence, the speedup scales linearly with the total temporal refinement ratio and similar runtime reduction behavior is observed when using iterative solver. The speedup on solving the linear system best represents the computational performance improvement. Since our problem size is small, the efficiency gain is not substantial when using direct solver. On the contrary, we observe 25 times speed up on solving the linear system when using iterative solver. Additional techniques on solving non-symmetric linear systems iteratively, such as relaxing linear solver tolerance using forcing function [14,28] and applying specialized preconditioners [12,16] for Krylov-based method, may be utilized for additional acceleration. Note that as we move towards more complex models such as 3-D black oil, the solution to the corresponding linear system is only accessible through iterative methods. Thus we should expect significant improvement on computational efficiency once we approach those types of problems.

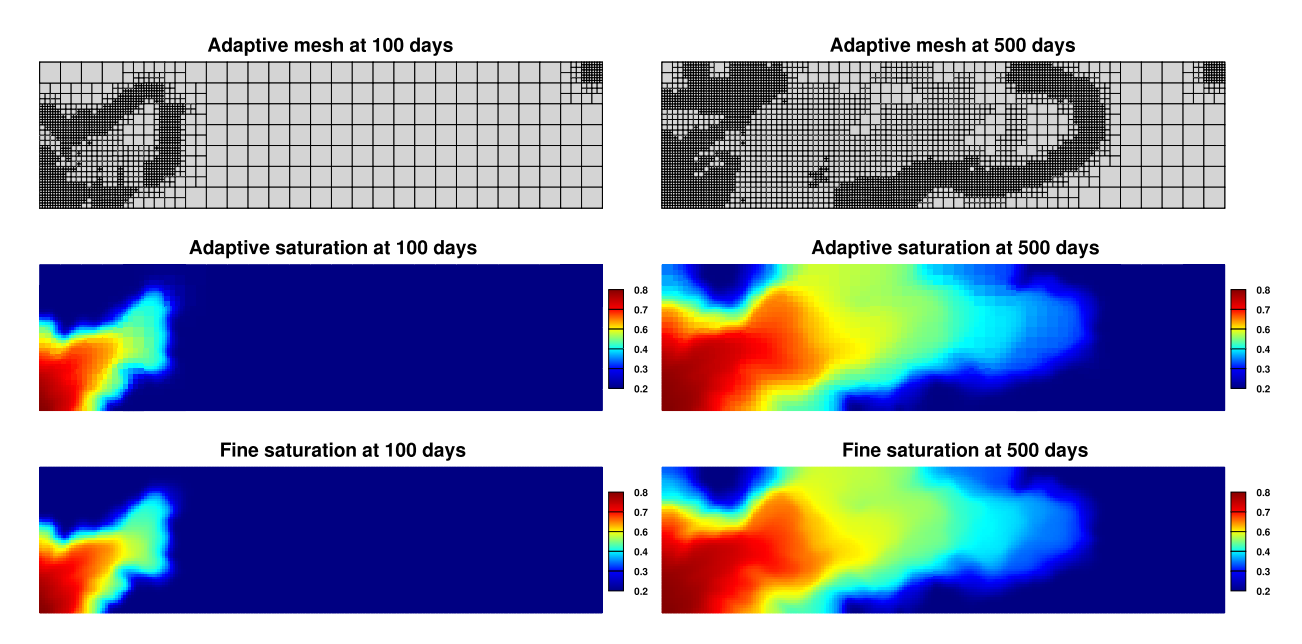


Fig. 11. Adaptive mesh (top) and water saturation profile (middle) generated by sequential refinement solver as compared to fine scale solution (bottom) at 100 and 500 days in Gaussian-like permeability field.

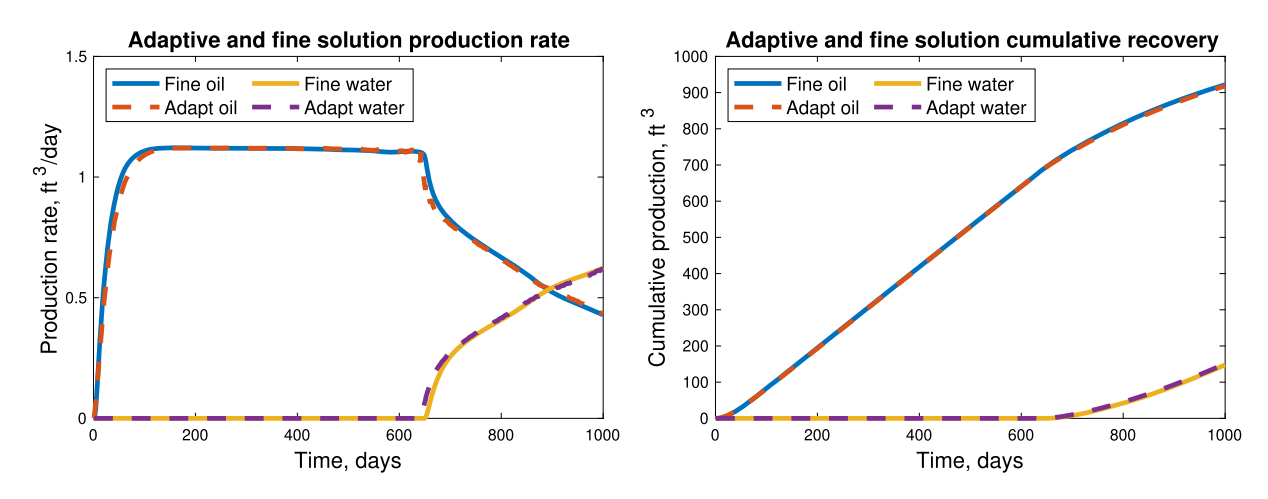


Fig. 12. Two phase production rates and cumulative recoveries from adaptive and fine scale solution of Gaussian-like permeability field.

5.2. Channelized permeability distribution

The channelized permeability field comes from SPE 10 dataset layer 52. The fine scale petrophysical data are shown in Fig. 14. We also allow three refinement levels in both space and time for this experiment and refinement ratio is also set to a factor of 2 between all levels. During numerical homogenization, we impose oversampling technique introduced by [11] and [13] to preserve channel connectivity as much as possible. The homogenized permeability distribution in X and Y direction is illustrated in Fig. 15. On the contrary to the Gaussian case, the upscaled channel permeability is highly anisotropic and many detailed structures are destroyed during the homogenization. Due to this condition, we apply an additional step to the refinement process for regions ahead of the saturation front. Subdomains with large variation between the fine and upscaled permeability are refined in space. This approach preserves the channel structure with minimum number of elements, similar to image compression with quadtree which aims to represent the image detail with minimum number of pixels, and thus ensures the correct pressure solution and flow direction beyond the saturation front. The computational domain is 56 ft \times 216 ft \times 1 ft \times 1000 days with coarsest and finest element size of 8 ft \times 8 ft \times 1 ft \times 10 days and 1 ft \times 1 ft

The adaptive water saturation profile with its mesh as compared to the fine scale solution at 200 and 400 days are plotted in Fig. 16. The overall saturation profile resembles each other between the two solutions. Here, the fine mesh not only concentrates at the water front, but also outlines the channel structure. The channel boundary is characterized

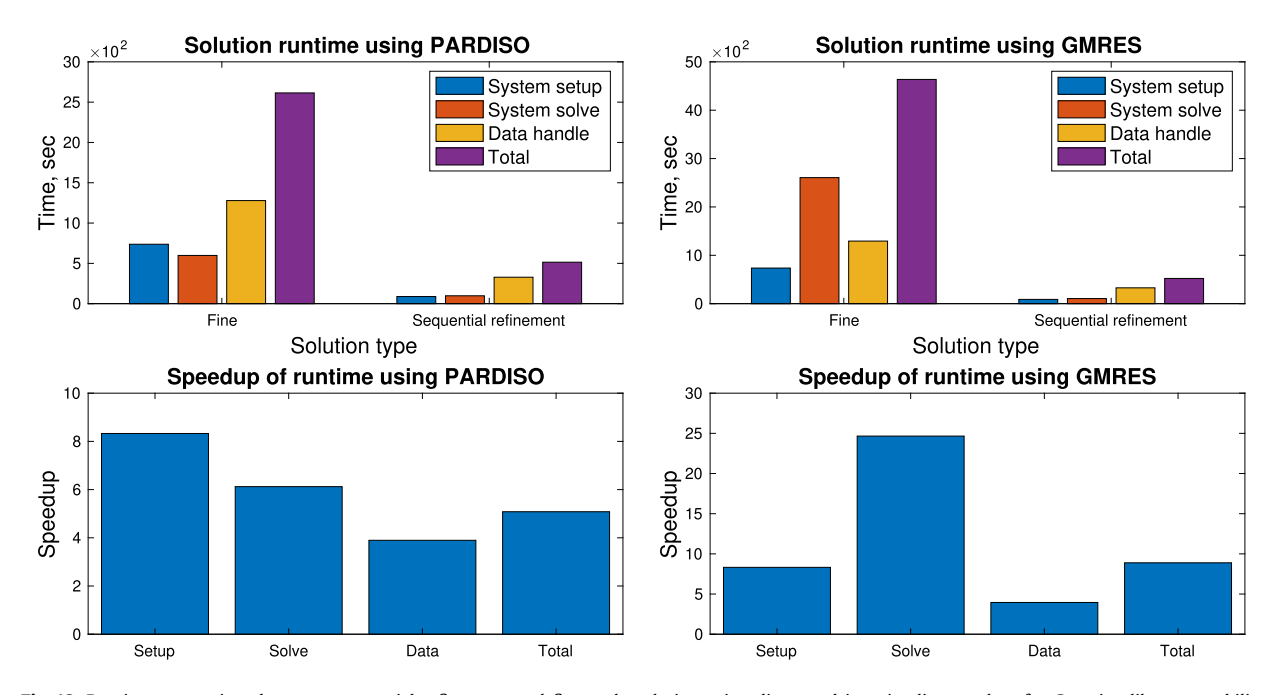


Fig. 13. Runtime comparison between sequential refinement and fine scale solution using direct and iterative linear solver for Gaussian-like permeability field.

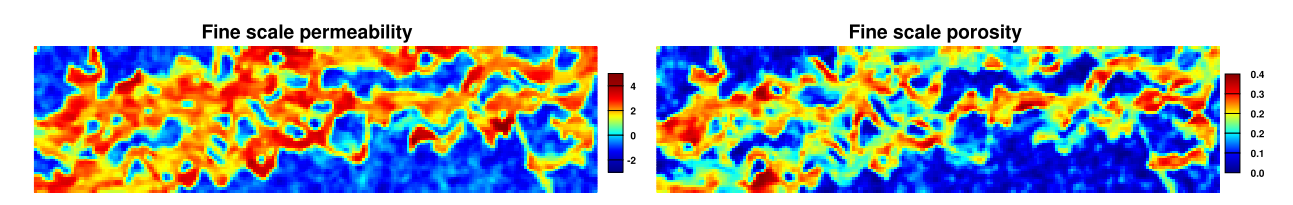


Fig. 14. Channelized fine scale permeability (left) and porosity (right) distribution.

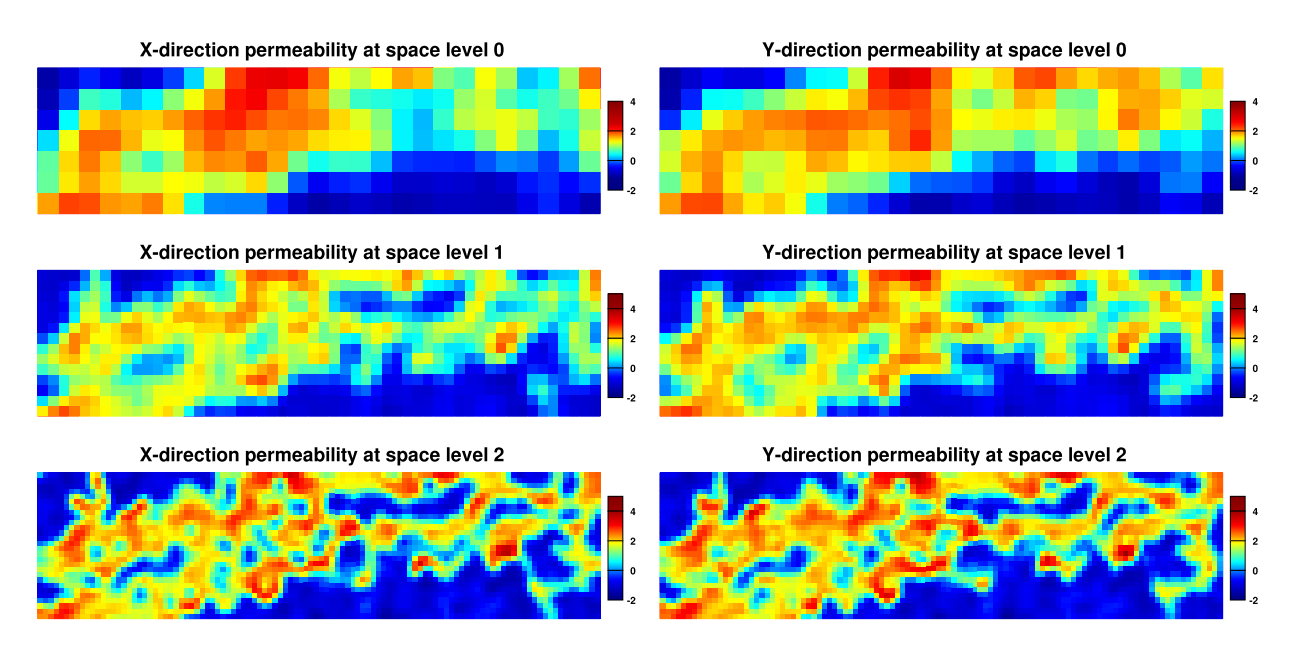


Fig. 15. Homogenized channel permeability in X and Y direction for each space level.

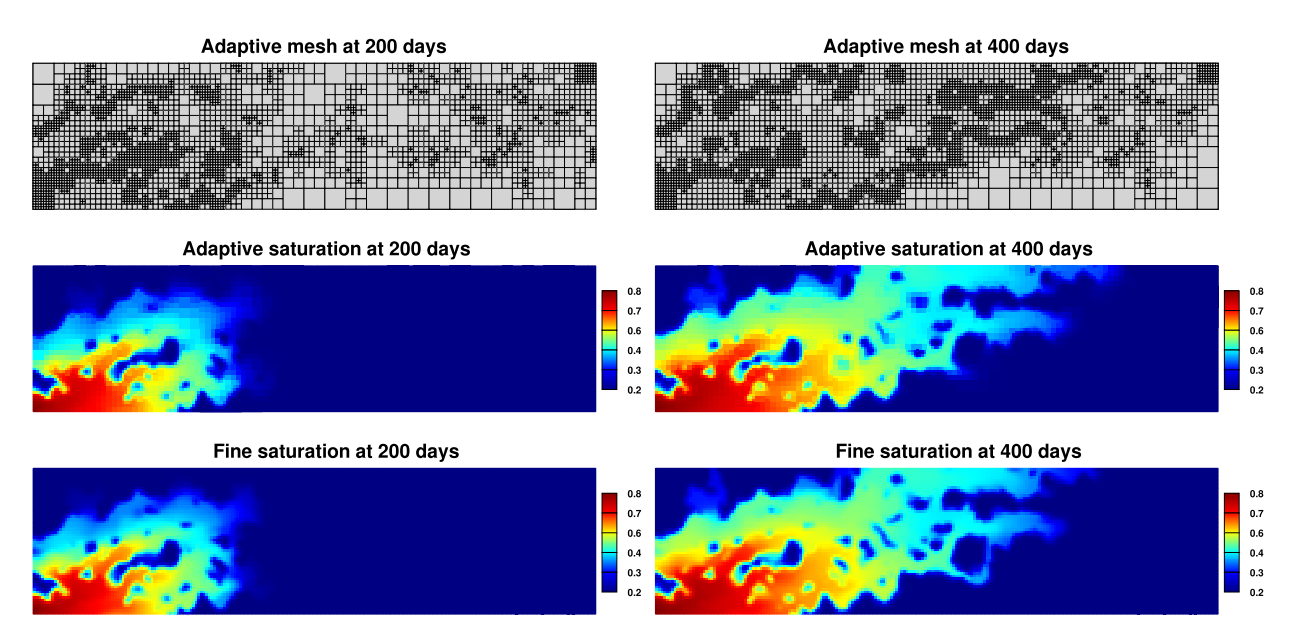


Fig. 16. Adaptive mesh (top) and saturation profile (middle) generated by sequential refinement solver as compared to fine scale solution (bottom) at 200 and 400 days in channelized permeability field.

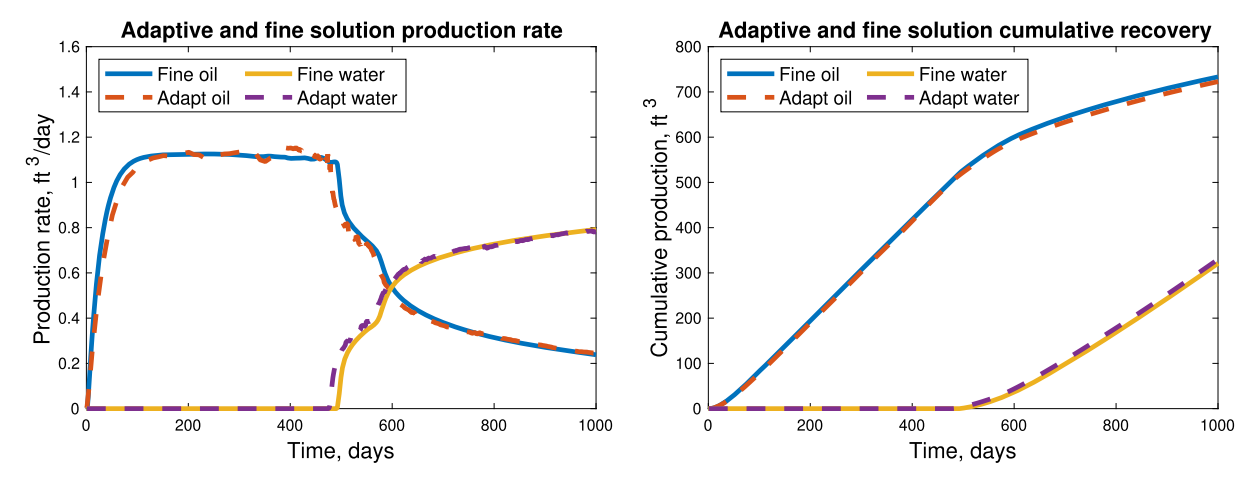


Fig. 17. Two phase production rates and cumulative recoveries from adaptive and fine solution of channelized permeability field.

by dramatic contrast of permeability, thus resulting in steep water saturation gradient. The refinement algorithm detects these features and deploys mesh with appropriate size accordingly. Many low permeability spots inside the main high permeability channel are also accurately identified and represented. Some subdomains beyond the saturation front are refined as well to recover necessary channel structure and ensures correction flow direction. Fig. 17 shows the production rates and cumulative recoveries of the two solutions. The adaptive and fine scale rates also look similar, however with obvious discrepancies. The rates from sequential refinement solver looks smoother than the fine scale solution at early time. It also suffers from slightly early water breakthrough. The oil and water cumulative production from the two solutions nearly overlap.

We also approach the solution by both direct and iterative method. The program execution time is shown in Fig. 18. The speedup on system setup and data handle also scales linearly with total temporal refinement ratio. The solution time reduction by direct solver remains low. We still observe a 25 times speedup using iterative solver, even when additional spatial refinements are applied beyond the saturation front. The substantial improvement is caused by two main reasons. First of all, the flow and transport is constrained within the channel structure behind the water front, making the saturation variation effectively zero in other part of the reservoir. Consequently, the number of grid cells required to represent the channel structure and saturation front is still relatively small, causing the adaptive solution easier to acquire. Secondly, the fine scale system consists of dramatic permeability contrast, resulting in the related linear system to have eigenvalues close

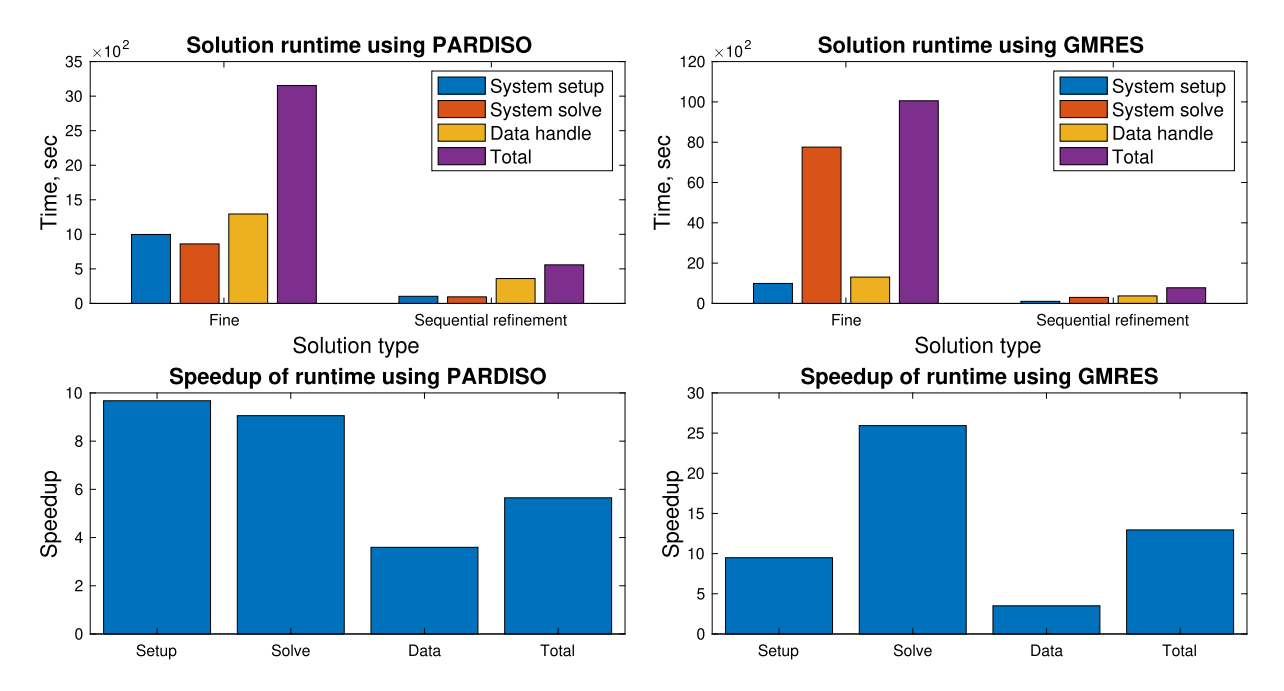


Fig. 18. Runtime comparison between sequential refinement and fine scale solution using direct and iterative linear solver for channelized permeability field

to zero. Solving such linear system with Krylov-based iterative methods requires many iterations, making the fine scale solution harder to obtain.

5.3. Compatibility with compressible flow

We also considered the compatibility of our algorithm to compressible flow using the same channelized permeability field presented in Fig. 14. The density calculation of compressible gas phase differs from the slightly compressible case Eqn. (2.5) as follows

$$\rho_g = \rho_{g,ref} \cdot (1 + c_g p_g) \tag{5.3}$$

This yields non-linearity due expansion which is no longer negligible. The compressibilities employed are 1×10^{-4} psi⁻¹ and 1×10^{-2} psi⁻¹ for liquid and gas respectively. In addition, the gas viscosity and density are significantly smaller than the ones for liquid. In this numerical study, the liquid viscosity is maintained as 3 [cp] while the gas viscosity has magnitude twice smaller (0.03 [cp]). The densities are chosen to be 53 lb/ft³ and 0.01 lb/ft³. The initial pressure, gas injection rate and total simulation time is adjusted to be 2500 psi, 10 ft³/day and 500 days.

The adaptive gas saturation profile with corresponding mesh as compared to the fine scale solution at 100 and 200 days are plotted in Fig. 19. The mesh structure is similar to the one in the previous slightly compressible case and the overall saturation profile for the two solutions coincide. Fig. 20 shows the production rates and cumulative recoveries of the two solutions. The adaptive and fine scale rates also look similar. However, the gas rate from the sequential refinement solver suffers from slightly early breakthrough. The cumulative production of the two phases for the both solutions almost overlap. The computational speedup for this compressible case is almost identical to the ones presented above.

6. Conclusions

We have introduced an algorithm that constructs adaptive mesh using error estimators to solve non-linear two-phase flow problems with reduced execution time. The procedure sequentially refines the mesh from coarsest to finest resolution in large non-linearity regions, with temporal and spatial adaptivity separated to accurately expose features in the system with relatively small number of elements, while ensuring numerical convergence. After each refinement, the initial guess for the new mesh is generated by the solution on the previous mesh through linear projection, which accelerates convergence rate. Results from two numerical experiments for slightly compressible flow are demonstrated. Rates and cumulative production from both experiments resembles well between the adaptive and fine scale solution. The water saturation profiles also look similar. We observe approximately 25 times speedup in solution time for the Gaussian-like and the channelized permeability field. The channel case suffers from a slightly early water breakthrough, which could be mitigated by loosening

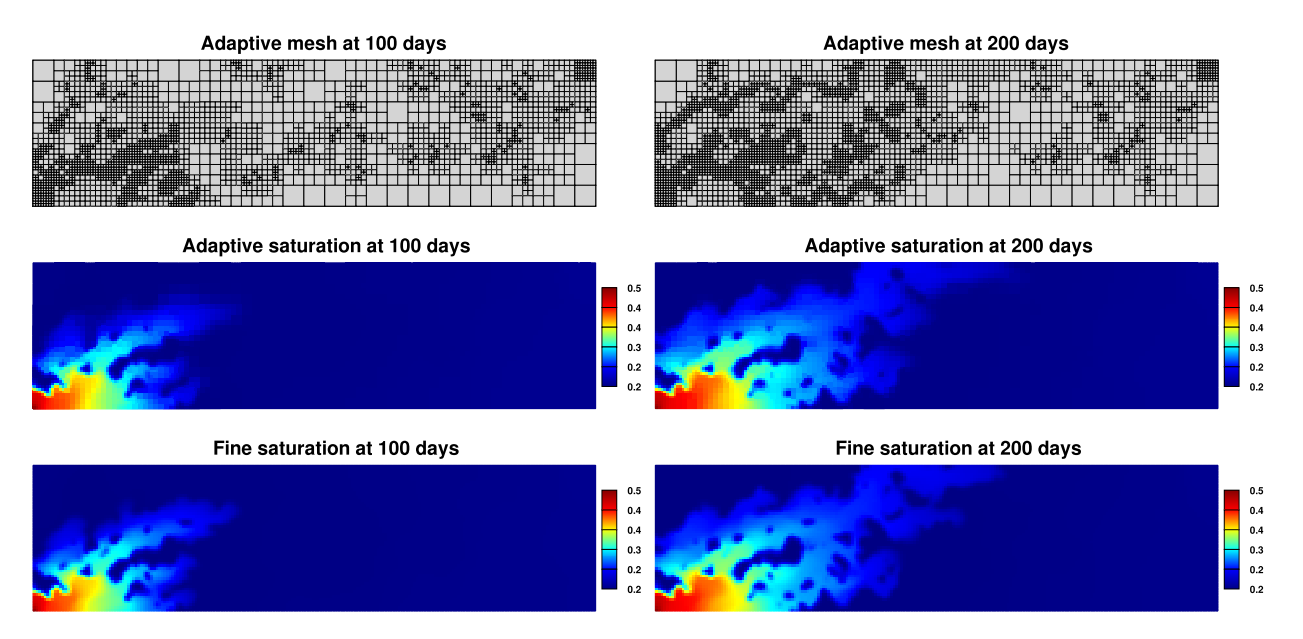


Fig. 19. Adaptive mesh (top) and saturation profile (middle) generated by sequential refinement solver as compared to fine scale solution (bottom) at 100 and 200 days in channelized permeability field for compressible flow.

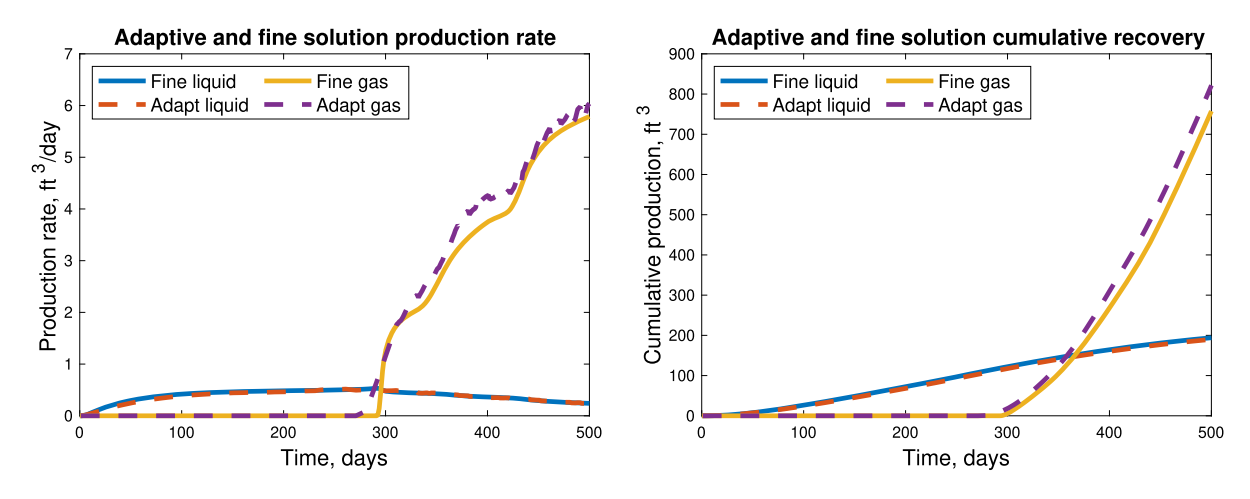


Fig. 20. Two phase production rates and cumulative recoveries from adaptive and fine solution of channelized permeability field.

refinement criterion. We also tested the algorithm for compressible flow and observed similar solution accuracy and computational speedup. With the promising results from two-phase flow problems, we propose to further test our algorithm on more complex models such as 3-D three-phase black oil system.

Declaration of competing interest

The authors declare that they have no known competing financial interests or personal relationships that could have appeared to influence the work reported in this paper.

Acknowledgement

The author would like to thank the Center for Subsurface Modeling for supporting this research. We would also like to extend our appreciation to Gurpreet Singh, Uwe Köcher and Ben Ganis for discussions on space-time strategies.

Appendix A. Fully discrete formulation

Consider the oil-water system, the variational form of Eqn. (2.1) through (2.4) is: find $\boldsymbol{u}_{\alpha,h}^n \in \boldsymbol{V}_h^{n,*}$, $\tilde{\boldsymbol{u}}_{\alpha,h}^n \in \boldsymbol{V}_h^{n,*}$, $s_{w,h}^n \in \boldsymbol{W}_h^n$, $p_{o,h}^n \in \boldsymbol{W}_h^n$ such that

$$\left(\frac{\partial}{\partial t}\phi\left(\rho_{w}s_{w,h}^{n}+\rho_{o}(1-s_{w,h}^{n})\right),w\right)+\left(\nabla\cdot\left(\boldsymbol{u}_{w,h}^{n}+\boldsymbol{u}_{o,h}^{n}\right),w\right)=\left(q_{w}+q_{o},w\right)$$
(A.1)

$$\left(\frac{\partial}{\partial t} \left(\phi \rho_{w} s_{w,h}^{n}\right), w\right) + \left(\nabla \cdot \boldsymbol{u}_{w,h}^{n}, w\right) = \left(q_{w}, w\right) \tag{A.2}$$

$$\left(K^{-1}\tilde{\boldsymbol{u}}_{o,h}^{n},\boldsymbol{v}\right) - \left(p_{o,h}^{n},\nabla\cdot\boldsymbol{v}\right) = 0\tag{A.3}$$

$$\left(K^{-1}\tilde{\boldsymbol{u}}_{w,h}^{n},\boldsymbol{v}\right) - \left(p_{w,h}^{n},\nabla\cdot\boldsymbol{v}\right) = -\left(p_{c},\nabla\cdot\boldsymbol{v}\right) \tag{A.4}$$

for all $\mathbf{v} \in \mathbf{V}_h^{n,*}$ and $w \in W_h^n$. The conversion between auxiliary and actual phase flux is referred to Eq. (2.11). The oil saturation and water pressure are eliminated by the saturation constrain and the capillary pressure relation (assume oil phase being the non-wetting phase).

For the fully discrete formulation, we will start by stating the basis functions in $RT_0 \times DG_0$ discretization scheme. In spatial dimensions, the pressure and saturation are piecewise constants while velocity is piecewise linear. Meanwhile all variables are piecewise constants in temporal dimension as stated in Section 2. To better present the discretized form, in this section, let $E_i^m = (\tau_m, \tau_{m+1}] \times F_i$ be a space-time element, we have

$$w_i^m = \begin{cases} 1 & \text{on } E_i^m = \tau_m < t \le \tau_{m+1} \bigcap x_{i-\frac{1}{2}} \le x \le x_{i+\frac{1}{2}} \\ 0 & \text{otherwise} \end{cases}$$
 (A.5)

$$\boldsymbol{\varphi}_{i+\frac{1}{2}}^{m} = \begin{cases} \frac{x - x_{i-\frac{1}{2}}}{\left|E_{i}^{m}\right|} & \text{on } E_{i}^{m} \\ \frac{x_{i+\frac{3}{2}} - x}{\left|E_{i+1}^{m}\right|} & \text{on } E_{i+1}^{m} \end{cases}$$
(A.6)

The solution to Eqn. (A.1) through (2.11) can be written in discrete form using basis functions as

$$\begin{cases} p_{0} = \sum_{m=1}^{q} \sum_{i=1}^{r} P_{i}^{m} w_{i}^{m} \\ s_{w} = \sum_{m=1}^{q} \sum_{i=1}^{r} S_{w,i}^{m} w_{i}^{m} \\ \mathbf{u}_{\alpha} = \sum_{m=1}^{q} \sum_{i=1}^{r+1} U_{\alpha,i+\frac{1}{2}}^{m} \boldsymbol{\varphi}_{i+\frac{1}{2}}^{m} \\ \tilde{\mathbf{u}}_{\alpha} = \sum_{m=1}^{q} \sum_{i=1}^{r+1} \tilde{U}_{\alpha,i+\frac{1}{2}}^{m} \boldsymbol{\varphi}_{i+\frac{1}{2}}^{m} \end{cases}$$
(A.7)

We remove the superscript n and subscript h in the above solution variables for this section since we need to use n to pair basis functions. While keeping the solution in discrete form, we now substitute the testing functions in the variational forms of mass conservation and constitutive equation with w_j^n and $\varphi_{j+\frac{1}{2}}^n$. For the first term in Eqn. (A.3) and (A.4) we obtain

$$\left(K^{-1}\tilde{\boldsymbol{u}}_{\alpha},\boldsymbol{\varphi}_{j+\frac{1}{2}}^{n}\right)_{\Omega\times J} = \left(K^{-1}\sum_{m=1}^{q}\sum_{i=1}^{r+1}\tilde{U}_{\alpha,i+\frac{1}{2}}^{m}\boldsymbol{\varphi}_{i+\frac{1}{2}}^{n},\boldsymbol{\varphi}_{j+\frac{1}{2}}^{n}\right)_{\Omega\times J} = \frac{1}{2\left|\boldsymbol{e}_{j+\frac{1}{2}}^{n}\right|}\left(\frac{x_{j+\frac{1}{2}}-x_{j-\frac{1}{2}}}{K_{j}} + \frac{x_{j+\frac{3}{2}}-x_{j+\frac{1}{2}}}{K_{j+1}}\right)\tilde{U}_{\alpha,j+\frac{1}{2}}^{n} \tag{A.8}$$

Here, $\left|e_{j+\frac{1}{2}}^n\right|$ is an edge of a space-time element. Since the framework uses backward Euler scheme in time to avoid Courant-Fredricks-Levy condition, we have the construction

$$\varphi_{i+\frac{1}{2}}^{m}(e_{j+\frac{1}{2}}^{n}) = \begin{cases} \frac{1}{\left|e_{j+\frac{1}{2}}^{n}\right|} & \text{as } i = j \text{ and } m = n\\ 0 & \text{otherwise} \end{cases}$$
(A.9)

The second term in Eqn. (A.3) and (A.4) can be reformulated as

$$(p_{\alpha}, \nabla \cdot \boldsymbol{\varphi}_{j+\frac{1}{2}}^{n})_{\Omega \times J} = \left(\sum_{m=1}^{q} \sum_{i=1}^{r} P_{\alpha,i}^{m} w_{i}^{m}, \nabla \cdot \boldsymbol{\varphi}_{j+\frac{1}{2}}^{n} \right)_{\Omega \times J} = \int_{E_{i}^{n}} \frac{P_{\alpha,j}^{n}}{|E_{j}^{n}|} - \int_{E_{i+1}^{n}} \frac{P_{\alpha,j+1}^{n}}{|E_{j+1}^{n}|} = P_{\alpha,j}^{n} - P_{\alpha,j+1}^{n}$$
(A.10)

When non-matching grid caused by different time scales at $(j+\frac{1}{2})^-$ and $(j+\frac{1}{2})^+$ is encountered, assume the ratio between coarse and fine time step to be $\frac{\delta t_c}{\delta l_f} = \ell$, then for each $0 \le k \le \ell - 1$

$$\left(p_{\alpha}, \nabla \cdot \boldsymbol{\varphi}_{j+\frac{1}{2}}^{n-\frac{1}{\ell}k}\right)_{\Omega \times J} = \left(\sum_{m=1}^{q} \sum_{i=1}^{r} P_{\alpha,i}^{m} w_{i}^{m}, \nabla \cdot \boldsymbol{\varphi}_{j+\frac{1}{2}}^{n-\frac{1}{\ell}k}\right)_{\Omega \times J} = P_{\alpha,j}^{n-\frac{1}{\ell}k} - P_{\alpha,j+1}^{n}$$

$$(A.11)$$

The variational form of capillary pressure term can be revised in similar way as Eqn. (A.10) and (A.11). Now we evaluate the mass conservation equation. The first term in Eqn. (A.2) becomes

$$\left(\frac{\partial}{\partial t} \sum_{m=1}^{q} \sum_{i=1}^{r} \phi \rho_{w} s_{w,i}^{m} w_{i}^{m}, w_{j}^{n}\right)_{\Omega \times J} = \left(\left(\phi \rho_{w} S_{w}\right)_{j}^{n} - \left(\phi \rho_{w} S_{w}\right)_{j}^{n-1}\right) \left|E_{j}^{n-1}\right| \tag{A.12}$$

In fine time scales, Eqn. (A.12) can be altered as follows.

$$\left(\frac{\partial}{\partial t} \sum_{m=1}^{q} \sum_{i=1}^{r} \phi \rho_{w} s_{w,i}^{m} w_{i}^{m}, w_{j}^{n-\frac{1}{\ell}k}\right)_{\Omega \times I} = \left(\left(\phi \rho_{w} S_{w}\right)_{j}^{n-\frac{1}{\ell}k} - \left(\phi \rho_{w} S_{w}\right)_{j}^{n-\frac{1}{\ell}(k+1)}\right) \left| E_{j}^{n-\frac{1}{\ell}(k+1)} \right|$$
(A.13)

The second term is calculated as

$$(\nabla \cdot \boldsymbol{u}_{w}, w_{j}^{n})_{\Omega \times J} = \left(\nabla \cdot \sum_{m=1}^{q} \sum_{i=1}^{r+1} U_{\alpha, i+\frac{1}{2}}^{m} \boldsymbol{\varphi}_{i+\frac{1}{2}}^{m}, w_{j}^{n}\right)_{\Omega \times J} = U_{w, j+\frac{1}{2}}^{n} - U_{w, j-\frac{1}{2}}^{n}$$
(A.14)

The approach to handle non-matching grid is a little different for this term. Assume the fine time partition stays on $(j+\frac{1}{2})^-$ side, then on fine time elements we have

$$(\nabla \cdot \boldsymbol{u}_{w}, w_{j}^{n-\frac{1}{\ell}k}) = U_{w,j+\frac{1}{2}}^{n-\frac{1}{\ell}k} - U_{w,j-\frac{1}{2}}^{n-\frac{1}{\ell}k}$$
(A.15)

while for the coarse time element we have

$$(\nabla \cdot \boldsymbol{u}_{w}, w_{j+1}^{n}) = U_{w,j+\frac{3}{2}}^{n} - \sum_{k=0}^{\ell-1} U_{w,j+\frac{1}{2}}^{n-\frac{1}{\ell}k}$$
(A.16)

Eqn. (A.13) and (A.16) will cause the accumulation and transmissibility matrix to have extra temporal bands forming in the lower triangle, making the corresponding linear system non-symmetric. The oil phase mass conservation equation is similar. Combining the equations for both phases will provide the expression for the total mass conservation equation. The two sides of Eqn. (2.11) is estimated as

$$(\mathbf{u}_{\alpha}, \mathbf{v}) = \sum_{m=1}^{q} \sum_{i=1}^{r+1} U_{\alpha, i+\frac{1}{2}}^{m} \left(\mathbf{\varphi}_{i+\frac{1}{2}}^{m}, \mathbf{\varphi}_{j+\frac{1}{2}}^{n} \right) = \frac{x_{j+\frac{3}{2}} - x_{j-\frac{1}{2}}}{2 \left| e_{j+\frac{1}{2}}^{n} \right|} U_{\alpha, j+\frac{1}{2}}^{n}$$
(A.17)

$$(\lambda_{\alpha}\tilde{\boldsymbol{u}}_{\alpha},\boldsymbol{v}) \approx (\lambda_{\alpha}^{*}\tilde{\boldsymbol{u}}_{\alpha},\boldsymbol{v}) = \frac{x_{j+\frac{3}{2}} - x_{j-\frac{1}{2}}}{2|e_{j+\frac{1}{2}}^{n}|} \lambda_{\alpha,j+\frac{1}{2}}^{*,n} \tilde{U}_{\alpha,j+\frac{1}{2}}^{n}$$

$$(A.18)$$

The $\lambda_{\alpha,j+\frac{1}{2}}^{*,n}$ is the upwind mobility for stable numerical solution and is defined as

$$\lambda_{\alpha,j+\frac{1}{2}}^{*,n} = \rho_{\alpha,j+\frac{1}{2}}^{n} \frac{k_{r\alpha,j+\frac{1}{2}}^{*}}{\mu_{\alpha}} = \begin{cases} \frac{1}{2\mu_{\alpha}} (\rho_{\alpha,j}^{n} + \rho_{\alpha,j+1}^{n}) k_{r\alpha} (S_{\alpha,j}^{n}) & \text{if } \tilde{U}_{\alpha,j+\frac{1}{2}}^{n} > 0\\ \frac{1}{2\mu_{\alpha}} (\rho_{\alpha,j}^{n} + \rho_{\alpha,j+1}^{n}) k_{r\alpha} (S_{\alpha,j+1}^{n}) & \text{otherwise} \end{cases}$$
(A.19)

The matrix corresponding to the above discrete formulation has sparsity pattern of three, five or seven non-zero diagonals, depending on the spatial dimension of the problem, with one extra temporal diagonal in the lower triangle. Forming such matrix in block format is referred to [17,33,35].

References

- [1] R. Abedi, B. Petracovici, R. Haber, A space–time discontinuous Galerkin method for linearized elastodynamics with element-wise momentum balance, Comput. Methods Appl. Mech. Eng. 195 (May 2006) 3247–3273.
- [2] Y. Amanbek, A New Adaptive Modeling of Flow and Transport in Porous Media Using an Enhanced Velocity Scheme, Ph.D. thesis, The University of Texas at Austin. 2018.
- [3] Y. Amanbek, G. Singh, M. Wheeler, Recovery of the interface velocity for the incompressible flow in enhanced velocity mixed finite element method, arXiv e-prints, arXiv:1901.04401, Jan 2019.
- [4] Y. Amanbek, G. Singh, M. Wheeler, H. Van Duijn, Adaptive numerical homogenization for upscaling single phase flow and transport, J. Comput. Phys. 387 (June 2019) 117–133.
- [5] Y. Amanbek, M. Wheeler, A priori error analysis for transient problems using enhanced velocity approach in the discrete-time setting, J. Comput. Appl. Math. 361 (Dec 2019) 459–471.
- [6] T. Arbogast, D. Estep, B. Sheehan, S. Tavener, A posteriori error estimates for mixed finite element and finite volume methods for parabolic problems coupled through a boundary, SIAM/ASA J. Uncertain. Quantificat. 3 (1) (Feb 2015) 169–198.
- [7] M. Bause, U. Köcher, Variational time discretization for mixed finite element approximations of nonstationary diffusion problems, J. Comput. Appl. Math. 289 (Dec 2015) 208–224.
- [8] M. Bause, F. Radu, U. Köcher, Space-time finite element approximation of the Biot poroelasticity system with iterative coupling, Comput. Methods Appl. Mech. Eng. 320 (June 2017) 745–768.
- [9] M. Christie, M. Blunt, Tenth SPE comparative solution project: a comparison of upscaling techniques, SPE Reserv. Eval. Eng. 4 (04) (Aug 2001) 308–317.
- [10] C. Chueh, M. Secanell, W. Bangerth, N. Djilali, Multi-level adaptive simulation of transient two-phase flow in heterogeneous porous media, Comput. Fluids 39 (9) (Oct 2010) 1585–1596.
- [11] E. Chung, Y. Efendiev, T. Hou, Adaptive multiscale model reduction with generalized multiscale finite element methods, J. Comput. Phys. 320 (Sept 2016) 69–95.
- [12] C. Dawson, H. Klie, M. Wheeler, C. Woodward, A parallel, implicit, cell-centered method for two-phase flow with a preconditioned Newton-Krylov solver, Comput. Geosci. 1 (Sept 1997) 215–249.
- [13] Y. Efendiev, T. Hou, Multiscale Finite Element Methods: Theory and Applications, vol. 4, Springer Science and Business Media, 2009.
- [14] S. Eisenstat, H. Walker, Choosing the forcing terms in an inexact Newton method, SIAM J. Sci. Comput. 17 (1) (Jan 1996) 16-32.
- [15] R. Finkel, J. Bentley, Quad trees a data structure for retrieval on composite keys, Acta Inform. 4 (1) (Mar 1974) 1-9.
- [16] A. Franceschini, N. Castelletto, M. Ferronato, Block preconditioning for fault/fracture mechanics saddle-point problems, Comput. Methods Appl. Mech. Eng. 344 (Feb 2019) 376–401.
- [17] B. Ganis, K. Kumar, G. Pencheva, M. Wheeler, A global Jacobian method for mortar discretizations of a fully implicit two-phase flow model, Multiscale Model. Simul. 12 (4) (Oct 2014) 1401–1423.
- [18] B. Ganis, G. Pencheva, M. Wheeler, Adaptive mesh refinement with an enhanced velocity mixed finite element method on semi-structured grids using a fully coupled solver, Comput. Geosci. 23 (1) (Feb 2019) 149–168.
- [19] M. Griebel, D. Oeltz, A sparse grid space-time discretization scheme for parabolic problems, Computing 81 (Oct 2007) 1-34.
- [20] T. Hoang, J. Jaffré, C. Japhet, M. Kern, J. Roberts, Space-time domain decomposition methods for diffusion problems in mixed formulations, SIAM J. Numer. Anal. 51 (6) (Dec 2013) 3532–3559.
- [21] T. Hoang, C. Japhet, M. Kern, J. Roberts, Space-time domain decomposition for advection–diffusion problems in mixed formulations, Math. Comput. Simul. 137 (July 2017) 366–389.
- [22] T. Hughes, G. Hulbert, Space-time finite element methods for elastodynamics: formulations and error estimates, Comput. Methods Appl. Mech. Eng. 66 (3) (Feb 1988) 339–363.
- [23] G. Hulbert, T. Hughes, Space-time finite element methods for second-order hyperbolic equations, Comput. Methods Appl. Mech. Eng. 84 (3) (Dec 1990) 377–348
- [24] C. Johnson, Numerical Solution of Partial Differential Equations by the Finite Element Method, 1st edition, Cambridge University Press, 1987.
- [25] U. Köcher, Variational Space-Time Methods for the Elastic Wave Equation and the Diffusion Equation, Ph.D. thesis, Helmut-Schmidt-University, 2015.
- [26] U. Köcher, M. Bause, Variational space-time methods for the wave equation, J. Sci. Comput. 61 (2) (Nov 2014) 424-453.
- [27] D. Krause, R. Krause, Enabling local time stepping in the parallel implicit solution of reaction-diffusion equations via space-time finite elements on shallow tree meshes, Appl. Math. Comput. 277 (Mar 2016) 164–179.
- [28] S. Lacroix, Y. Vassilevski, J. Wheeler, M. Wheeler, Iterative solution methods for modeling multiphase flow in porous media fully implicitly, SIAM J. Sci. Comput. 25 (3) (Apr 2003) 905–926.
- [29] U. Langer, S. Moore, M. Neumüller, Space–time isogeometric analysis of parabolic evolution problems, Comput. Methods Appl. Mech. Eng. 306 (July 2016) 342–363.
- [30] H. Li, M. Wheeler, Sequential refinement solver using space-time domain decomposition for non-linear multiphase flow problems, arXiv e-prints, arXiv:1901.09436, lan 2019.
- [31] M. Peszyńska, M. Wheeler, I. Yotov, Mortar upscaling for multiphase flow in porous media, Comput. Geosci. 6 (1) (Mar 2006) 73–100.
- [32] G. Singh, W. Leung, M. Wheeler, Multiscale methods for model order reduction of non-linear multiphase flow problems, Comput. Geosci. (Nov 2018) 1–19.
- [33] G. Singh, G. Pencheva, M. Wheeler, An approximate Jacobian nonlinear solver for multiphase flow and transport, J. Comput. Phys. 375 (Dec 2018) 337–351.
- [34] G. Singh, M. Wheeler, A domain decomposition approach for local mesh refinement in space and time, in: SPE Annual Technical Conference and Exhibition, Society of Petroleum Engineers, Sept 2018.
- [35] G. Singh, M. Wheeler, A space-time domain decomposition approach using enhanced velocity mixed finite element method, J. Comput. Phys. 374 (Dec 2018) 893–911.
- [36] T. Tezduyar, S. Sathe, Enhanced-discretization space-time technique (EDSTT), Comput. Methods Appl. Mech. Eng. 193 (Apr 2004) 1385-1401.
- [37] S. Thomas, M. Wheeler, Enhanced velocity mixed finite element methods for modeling coupled flow and transport on non-matching multiblock grids, Comput. Geosci. 15 (4) (Sept 2011) 605–625.
- [38] M. Vohralik, M. Wheeler, A posteriori error estimates, stopping criteria, and adaptivity for two-phase flows, Comput. Geosci. 17 (5) (Oct 2013) 789-812.
- [39] J. Wheeler, M. Wheeler, I. Yotov, Enhanced velocity mixed finite element methods for flow in multiblock domains, Comput. Geosci. 6 (Jan 2002) 315–332.
- [40] H. Yu, A local space-time adaptive scheme in solving two-dimensional parabolic problems based on domain decomposition methods, SIAM J. Sci. Comput. 23 (1) (2001) 304–322.